

Article

Tungsten Oxide Morphology-Dependent Au/TiO₂/WO₃ Heterostructures with Applications in Heterogenous Photocatalysis and Surface-Enhanced Raman Spectroscopy

István Székely^{1,2,3} , Zoltán Kovács^{1,2,4}, Mihai Rusu^{2,5}, Tamás Gyulavári⁴ , Milica Todea^{2,6}, Monica Foçsan⁷ , Monica Baia^{2,3,8,*}  and Zsolt Pap^{2,3,4,*}

- ¹ Doctoral School of Physics, Babes-Bolyai University, M. Kogălniceanu 1, 400084 Cluj-Napoca, Romania; istvan.székely@ubbcluj.ro (I.S.); zoltan.kovacs@ubbcluj.ro (Z.K.)
- ² Centre of Nanostructured Materials and Bio-Nano Interfaces, Institute for Interdisciplinary Research on Bio-Nano-Sciences, Treboniu Laurian 42, 400271 Cluj-Napoca, Romania; mihai.rusu@phys.utcluj.ro (M.R.)
- ³ Laboratory for Advanced Materials and Applied Technologies, Institute for Research, Development and Innovation in Applied Natural Sciences, Fantanele 30, 400294 Cluj-Napoca, Romania
- ⁴ Department of Applied and Environmental Chemistry, University of Szeged, Rerrich Sqr. 1, HU-6720 Szeged, Hungary; gyulavarit@chem.u-szeged.hu
- ⁵ Department of Physics and Chemistry, Technical University of Cluj-Napoca, Memorandumului 28, 400114 Cluj-Napoca, Romania
- ⁶ Faculty of Medicine, Iuliu Hațieganu University of Medicine and Pharmacy, Victor Babeș 8, 400012 Cluj-Napoca, Romania
- ⁷ Nanobiophotonics and Laser Microspectroscopy Center, Interdisciplinary Research Institute on Bio-Nano-Sciences, Babes-Bolyai University, Treboniu Laurian 42, 400271 Cluj-Napoca, Romania; monica.iosin@ubbcluj.ro
- ⁸ Faculty of Physics, Babeș-Bolyai University, Mihail Kogălniceanu Str. 1, 400084 Cluj-Napoca, Romania
- * Correspondence: monica.baia@ubbcluj.ro (M.B.); zsolt.pap@ubbcluj.ro (Z.P.)



Citation: Székely, I.; Kovács, Z.; Rusu, M.; Gyulavári, T.; Todea, M.; Foçsan, M.; Baia, M.; Pap, Z. Tungsten Oxide Morphology-Dependent Au/TiO₂/WO₃ Heterostructures with Applications in Heterogenous Photocatalysis and Surface-Enhanced Raman Spectroscopy. *Catalysts* **2023**, *13*, 1015. <https://doi.org/10.3390/catal13061015>

Academic Editors: Detlef W. Bahnemann and Jorge Bedia

Received: 29 March 2023

Revised: 12 June 2023

Accepted: 15 June 2023

Published: 17 June 2023



Copyright: © 2023 by the authors. Licensee MDPI, Basel, Switzerland. This article is an open access article distributed under the terms and conditions of the Creative Commons Attribution (CC BY) license (<https://creativecommons.org/licenses/by/4.0/>).

Abstract: Developing highly efficient Au/TiO₂/WO₃ heterostructures with applications in heterogeneous photocatalysis (photocatalytic degradation) and surface-enhanced Raman spectroscopy (dye detection) is currently of paramount significance. Au/TiO₂/WO₃ heterostructures were obtained via heat or time-assisted synthesis routes developed by slightly modifying the Turkevich–Frens synthesis methods and were investigated by TEM, SEM, XRD, Raman spectroscopy, XPS, photoluminescence, and UV–vis DRS techniques. Structural features, such as WO₃ crystalline phases, TiO₂ surface defects, as well as the WO₃ (220) to TiO₂-A (101) ratio, were the key parameters needed to obtain heterostructures with enhanced photocatalytic activity for removing oxalic acid, phenol, methyl orange, and aspirin. Photodegradation efficiencies of 95.9 and 96.9% for oxalic acid; above 96% (except one composite) for phenol; 90.1 and 97.9% for methyl orange; and 81.6 and 82.1% for aspirin were obtained. By employing the SERS technique, the detection limit of crystal violet dye, depending on the heterostructure, was found to be between 10^{−7}–10^{−8} M. The most promising composite was Au/TiO₂/WO₃-HW-TA it yielded conversion rates of 82.1, 95.9 and 96.8% for aspirin, oxalic acid, and phenol, respectively, and its detection limit for crystal violet was 10^{−8} M. Au/TiO₂/WO₃-NWH-HA achieved 90.1, 96.6 and 99.0% degradation efficiency for methyl orange, oxalic acid, and phenol, respectively, whereas its limit of detection was 10^{−7} M. The Au/TiO₂/WO₃ heterojunctions exhibited excellent stability as SERS substrates, yielding strong-intensity Raman signals of the pollutant molecules even after a long period of time.

Keywords: heterostructures; aspirin; toxic pollutants; photocatalytic activity; Au NPs; crystal violet; SERS; detection; limit of detection

1. Introduction

In recent decades, Au/TiO₂/WO₃ ternary heterostructures have been studied due to their broad applicability in heterogeneous photocatalysis and surface-enhanced Raman

spectroscopy (SERS); these promising composites are being employed for wastewater remediation [1], photocatalytic degradation [2], H₂ evolution [3], CO₂ reduction [4], photovoltaic devices [5], and dye detection via SERS [6].

M. M. Rhaman et al. synthesized Au/TiO₂/WO₃ heterojunctions by photo-depositing Au NPs on the surface of TiO₂/WO₃ heterostructures. They investigated the efficiency of the photocatalyst under Vis light irradiation and found that bare TiO₂ and WO₃ were not photoactive, but that TiO₂/WO₃ heterostructures removed 52% of phenol (PHE) and 42% of methylene blue (MB). The Au/TiO₂/WO₃ composites (0.25% Au) efficiently removed 63% of PHE and 52% of MB [1]. X. Yang et al. developed novel Au/TiO₂/WO₃ heterostructures to study their photocatalytic efficiency under solar light irradiation. The Au NPs were deposited through chemical reduction (NaBH₄), and their average particle size was ≈10 nm. The photoactivity of the composites was assessed by removing MB. TiO₂ efficiently removed 51.3% of MB, and the Au/TiO₂/WO₃ heterostructures achieved 75.6% (0.4% Au), 94.5% (1% Au), and 88.9% of MB (3% Au) efficiency [2].

M. Tahir et al. embedded Au NPs onto WO₃/TiO₂ nanocomposites and employed Au/TiO₂/WO₃ heterojunctions for enhanced H₂ evolution. The heterojunctions' Au content varied between 0.3% and 0.7%, and the most significant volume of H₂ (17,200 ppm·h⁻¹·g_{catalyst}⁻¹) was produced with 0.5% Au and glycerol as the sacrificial reagent. The heterojunction was almost sixfold more efficient than the pristine TiO₂ sample [3].

Z. Zhu et al. prepared bimetallic Pd–Au/TiO₂/WO₃ nanocomposites with various Pd and Au percentages and studied their potential to reduce CO₂ to CH₄ and CO under Vis light exposure. The noble metal nanoparticles (of ≈10 nm size) were simultaneously deposited on the TiO₂/WO₃ composites via impregnation. The best three performing heterostructures were Pd–Au (0.5–0.3 wt.%)/TiO₂/WO₃, Pd (0.5 wt.%)/TiO₂/WO₃, and Pd–Au (0.5–0.1 wt.%)/TiO₂/WO₃, which yielded 11.3, 15.1 and 39.1 μmol·g⁻¹·h⁻¹ of CH₄, respectively, and 224.4, 225.5 and μmol·g⁻¹·h⁻¹ of CO [4]. M. K. Akbari et al. prepared two-dimensional Au/TiO₂/WO₃ heterojunctions using atomic layer deposition (ALD) and studied their potential application as photovoltaic devices. The photoresponse was 15 mA·W⁻¹ under UV irradiation and 18 mA·W⁻¹ under Vis light irradiation, while the external quantum efficiency (EQE) was 6% and 4.5%. By obtaining 2D Au/TiO₂/WO₃ film heterojunctions with film thicknesses of 0.7 nm for WO₃ and 3.5 nm for TiO₂, the EQE of the heterojunctions was improved by 13.4% [5]. B. Zhang et al. obtained Au/TiO₂/WO₃ heterojunctions by electrodepositing Au NPs on TiO₂/WO₃ nanotube/nanoflower composites. The average particle size of the Au NPs was ≈35 nm. The obtained Au/TiO₂/WO₃ heterojunctions were employed for the SERS detection of dyes such as rhodamine 6G (R6G), crystal violet (CV), malachite green (MG), and alizarin (AZ). The heterojunctions' limit of detection (LoD) was 10⁻¹¹ M in the case of MG and CV, respectively, and 10⁻¹² M in the case of R6G and AZ dyes [6].

V. Iliev et al. prepared Au/TiO₂/WO₃ composites via photoreduction, using Au NPs that had an average particle size of 5 nm. The photocatalytic activity was assessed under UV and Vis irradiation for oxalic acid (OA), achieving degradation efficiencies of 82% and 10% [7]. Karácsonyi et al. synthesized Au/TiO₂/WO₃ composites using the photodeposition method, with an Au NP average size of 60–80 nm, and employed them for the photocatalytic removal of OA under UV radiation exposure, yielding efficiencies of 64.7 and 68.7% [8]. G. Kovács et al. and L. Baia et al. synthesized Au/TiO₂/WO₃ (metal oxide and aerogel-based) heterostructures via photoreduction (Au NPs' average size was ≈50 nm in both cases), and utilized the composites to remove PHE under UV and Vis exposure. The photocatalysts with 1% Au, 4% WO₃, and 95% TiO₂ composition were the most efficient under UV radiation exposure, yielding a PHE removal efficiency of 80% (metal oxide-based composites) [9] and a 60% aerogels removal efficiency [10].

J-B. Cai et al. obtained Au/TiO₂/WO₃ photocatalysts and studied their efficiency in removing trimesic acid (TMA) and Rhodamine B (RhB) under Vis irradiation. In this study, the Au NPs' average particle size was ≈20 nm and they were synthesized by the Turkevich–Frens method. The most widely employed method for reducing gold nanoparticles (Au

NPs) is the one Turkevich and coworkers developed due to its reliability, reproducibility, and Au NP uniformity [11–18]. The Au/TiO₂/WO₃ photocatalysts efficiently removed 95% of TMA and 94% of RhB, yielding enhanced photoactivity compared to TiO₂ (80% for TMA; 62% for RhB) [19].

M.M. Momeni et al. synthesized nanotube Au/TiO₂/WO₃ heterostructures via photodeposition and anodic oxidation. The obtained composites efficiently removed ≈90% of MB [20]. X. Wang et al. synthesized Au/TiO₂/WO₃ heterojunctions by loading single Au atoms electrochemically onto the oxygen vacancies (OVc) of WO₃. The Au/TiO₂/WO₃ heterojunctions photocatalytic activity was evaluated for toluene (TOL) removal under UV irradiation. The synthesized heterojunctions efficiently removed 94.5% of TOL and achieved 85.5% TOL mineralization [21].

A unique application possibility of Au/TiO₂/WO₃ is that the photocatalytic process can be monitored via SERS detection in real-time, and the composites can be used as a self-cleaning SERS substrate due to the in-situ degradation of pollutants. For the simultaneous in situ detection and photocatalytic degradation of pollutants, not only might the Au/TiO₂/WO₃ composites be suitable, but also other materials such as porous Au–Ag alloy particles inlaid AgCl membranes, Au NP-decorated Ag(Cl, Br) [Ag(Cl, Br)–Au] micro-necklaces, and arrayed AgCl micro-rods [22–24].

Even though several articles have been published regarding the synthesis of Au/TiO₂/WO₃ heterostructures with improved photoactivity and enhanced H₂ production, respectively, as SERS substrates for pollutant detection, up until now, Au/TiO₂/WO₃ heterojunctions have not been employed for the photocatalytic removal of multiple pollutants; therefore, as SERS substrates in the same study, they should be considered as the newest and strongest point of our manuscript.

Thus, throughout this study, we addressed the issue of optimizing Au/TiO₂/WO₃ heterojunctions in order to obtain materials that possess enhanced photocatalytic activity and are suitable as SERS substrates. The Au NPs were deposited on the TiO₂/WO₃ heterostructures' surface using a slightly modified Turkevich–Frens synthesis route. The optimization of the heterojunctions' structure was carried out by studying the effect of WO₃ with three different morphologies (prismatic dipyrmaid, microrods, and microflowers) and various crystalline structures (monoclinic, hexagonal partial hydrate, and the mixture of the two), respectively, by employing two different synthesis routes for the Au NP reduction. The best performing Au/TiO₂/WO₃ composites efficiently removed 96.6% of OA, 99.0% of PHE, 97.9% of methyl orange (MO) under UV exposure, and 82.1% of aspirin (ASP) under Vis light exposure. The obtained Au/TiO₂/WO₃ heterostructures can be employed as SERS-based sensors, as they detect crystal violet (CV) dye in low concentrations, with a limit of detection of 10^{−8} M.

2. Results

2.1. TEM Investigations

Based on the TEM micrographs of the Au/TiO₂/WO₃-HW heterojunctions (Figure S1), the presence of all three components can be observed. The morphology of the WO₃ that was hydrothermally synthesized by employing H₂WO₄ as a precursor (WO₃-HW component) was prismatic dipyrmaid-like, consisting of blade-like structures. The building blocks of the latter were nanoplates, which were formed layer by layer. The size of WO₃-HW was between 1–2 μm [25]. Commercial TiO₂ (Evonik Aeroxide P25) presented its typical morphology with a mixture of smaller (corresponding to anatase) and larger (corresponding to rutile) nanoparticles [26]. The morphology of the Au NPs was mainly spherical with a size distribution between 10–36 nm for Au/TiO₂/WO₃-HW–HA and 10–45 nm for Au/TiO₂/WO₃-HW–TA. SEM micrographs of the prismatic dipyrmaid WO₃-HW can be found in the Supplementary Materials (Figures S4 and S5).

All components of the ternary composites were present for the Au/TiO₂/WO₃-NWH samples, too (Figure S2). The morphology of the WO₃ that was hydrothermally synthesized by employing Na₂WO₄·2H₂O as a precursor (WO₃-NWH) was rod-like, and each rod was

thin (≈ 20 nm). The individual nanorods were stacked together to form bundles with a diameter between 100–150 nm and a length between 0.5–1.0 μm [27]. The morphology observed for the commercial titania was the same as described above (Figure S1). In this case, the morphology of the Au NPs was mostly spherical, and their size distribution was between 10–45 nm (for Au/TiO₂/WO₃-NWH–HA) and between 10–36 nm (for Au/TiO₂/WO₃-NWH–TA). SEM micrographs of the rod-like WO₃-NWH can be found in the Supplementary Materials (Figures S6 and S7).

Concerning Au/TiO₂/WO₃-AMT–HA and Au/TiO₂/WO₃-AMT–TA, each component in the ternary composite could be identified based on the TEM micrographs (Figure S3), but the morphology of the WO₃ that was hydrothermally synthesized by employing (NH₄)₆H₂W₁₂O₄₀·xH₂O as a precursor (WO₃-AMT) was challenging to determine. A flower-like morphology was observed based on the SEM micrographs of WO₃-AMT, with sizes between 3–4 μm . The micro-flowers comprised plates with a diameter between 250–500 nm. The plates were built of layered sheets with a diameter between 100–250 nm and a length of 1–2 μm . The morphology and particle size of the commercial TiO₂ were the same as in the previous two cases. The morphology of the Au NPs was generally spherical, with a size distribution between 10–55 nm for Au/TiO₂/WO₃-AMT–HA and between 12–36 nm for Au/TiO₂/WO₃-AMT–TA. SEM micrographs of the flower-like WO₃-AMT can be found in the Supplementary Materials (Figures S8 and S9). The particle size of Evonik Aeroxide P25 was below 100 nm.

The average diameters of the Au NPs presented the same trend for each WO₃ morphology (Table 1). That is, heat-assisted (HA) synthesis tended to result in relatively larger particle sizes (21.4–24.1 nm), whereas time-assisted (TA) synthesis tended to result in relatively smaller particle sizes (19.4–21 nm). The observed slight differences could appear because not all the HAuCl₄ solution was successfully reduced during the HA synthesis route (proven by the presence of Na and Cl in the EDX spectra of the samples). The EDX spectra of the heterostructures are available in the Supplementary Materials (Figures S10–S15). Since the synthesis time is considerably shorter in the HA route (4 h) than in the TA one (24 h), the suspension temperature also decreased in a relatively short period, thus favoring a larger particle size formation. In the TA synthesis route, the smaller average particle size could be due to the constant 25 °C room temperature and the prolonged synthesis duration (24 h). Both parameters can facilitate the reduction of uniform Au NPs and result in a greater amount of deposited Au NPs from the HAuCl₄ solution. These assumptions were proven using SEM–EDX measurements (Table 2). The elemental composition of the ternary composites also indicates that in the HA synthesis route, fewer Au NPs were deposited than in the TA synthesis route.

Table 1. The average diameter of gold nanospheres (determined based on TEM micrographs).

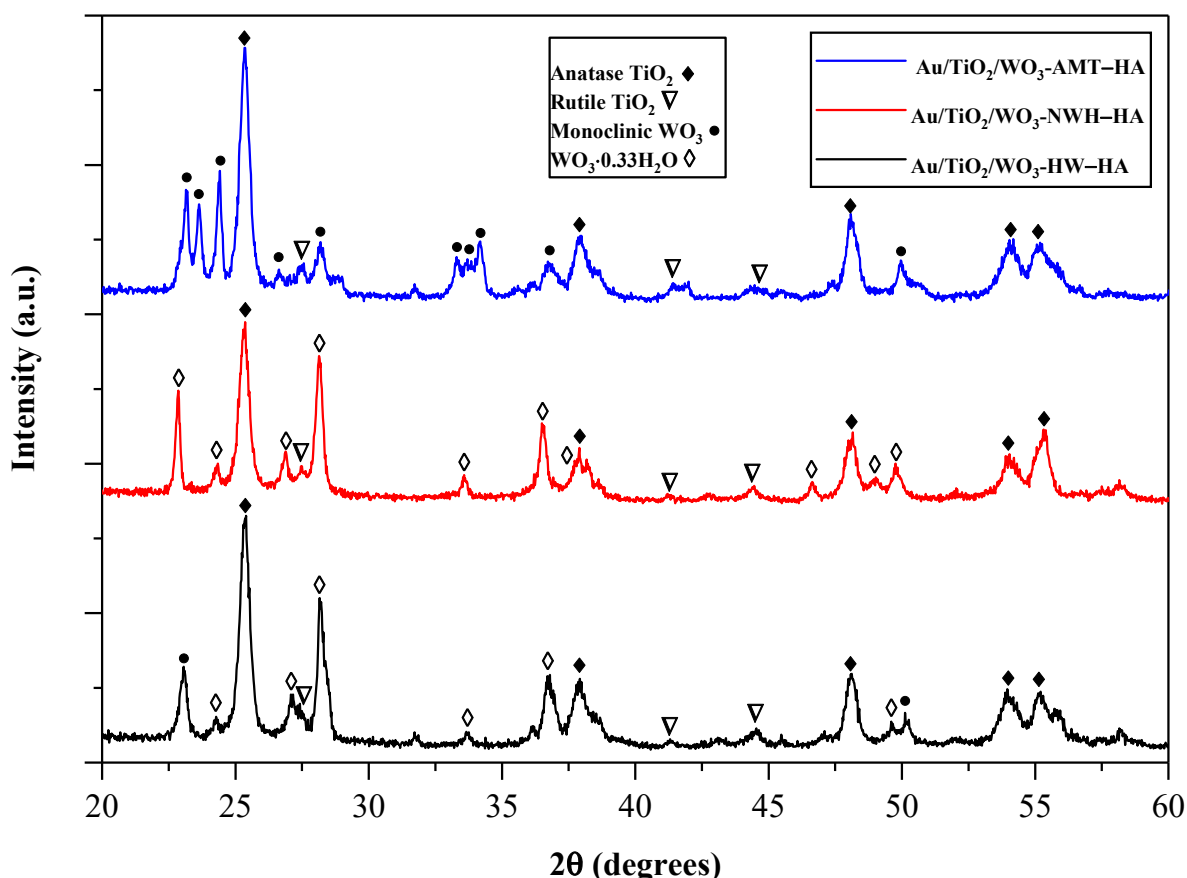
Sample	Diameter (nm)	Standard Deviation (SD)
Au/TiO ₂ /WO ₃ -HW–HA	21.4	± 5.2 nm
Au/TiO ₂ /WO ₃ -HW–TA	19.4	± 5.4 nm
Au/TiO ₂ /WO ₃ -NWH–HA	21.3	± 5.2 nm
Au/TiO ₂ /WO ₃ -NWH–TA	20.4	± 4.2 nm
Au/TiO ₂ /WO ₃ -AMT–HA	24.1	± 6.7 nm
Au/TiO ₂ /WO ₃ -AMT–TA	21.0	± 4.4 nm

2.2. X-ray Diffraction Analysis

The XRD patterns of the samples (Figures 1 and 2) proved the presence of TiO₂ and WO₃ in each composite. Concerning the commercial TiO₂, two crystal phases were identified: anatase (diffractions at 2θ : 25.4°, 37.1°, 48.0°, 53.9°, and 55.1°) and rutile (diffractions at 2θ : 27.5°, 41.4°, and 44.4°). Its crystal phase composition was 89% anatase (JCPDS card no. 21-1272) and 11% rutile (JCPDS card no. 21-1276), as expected [28,29].

Table 2. The average elemental composition of the ternary composites (SEM–EDX).

Sample	Elemental Composition (%)						
	Au	O	Na	Al	Cl	Ti	W
Au/TiO ₂ /WO ₃ -HW-HA	0.38	54.81	1.90	1.05	0.48	28.98	12.40
Au/TiO ₂ /WO ₃ -HW-TA	0.72	45.60	3.00	1.12	1.38	33.29	14.89
Au/TiO ₂ /WO ₃ -NWH-HA	0.34	48.26	1.00	2.68	0.27	37.54	9.91
Au/TiO ₂ /WO ₃ -NWH-TA	0.53	52.66	3.34	1.01	0.83	32.92	8.70
Au/TiO ₂ /WO ₃ -AMT-HA	0.65	48.02	1.25	0.68	0.68	38.76	9.96
Au/TiO ₂ /WO ₃ -AMT-TA	0.79	47.02	2.68	0.87	1.18	39.80	7.67

**Figure 1.** XRD patterns of the Au/TiO₂/WO₃ heterostructures obtained via the heat-assisted method.

Au/TiO₂/WO₃-HW-HA and Au/TiO₂/WO₃-HW-TA samples presented mixed crystal phases of WO₃, that is, WO₃·0.33H₂O partial hydrate (JCPDS card no. 35-1001) [30] and monoclinic WO₃ (γ-WO₃; JCPDS card no. 43-1035). The crystal phase composition was 90.6% WO₃·0.33H₂O partial hydrate and 9.3% monoclinic [31]. The corresponding diffractions for the first one were identified at 2θ: 28.2°, 33.58°, 36.6°, and 37.75°, while for the latter, at 2θ: 23.02°, and 49.98° [32]. In Au/TiO₂/WO₃-NWH-HA and Au/TiO₂/WO₃-NWH-TA, only the WO₃·0.33H₂O partial hydrate (JCPDS card no. 35-1001) could be identified in both samples at 2θ: 22.86°, 24.34°, 26.88°, 28.2°, 33.58°, 36.5°, 37.7°, 46.1°, and 49.76°. In Au/TiO₂/WO₃-AMT-HA and Au/TiO₂/WO₃-AMT-TA, only the monoclinic WO₃ crystal phase (JCPDS card no. 43-1035) could be identified at 2θ: 23.4°, 23.64°, 24.42°, 26.64°, 28.2°, 33.3°, 33.7°, 34.18°, 36.72°, 44.48°, and 49.96°. Depending on the synthesis of Au deposition, changes in the crystal structure may occur, as the deposition is influenced by the metal oxides' morphology [33–35]. The modifications to the crystal structures were confirmed by the changes in the ratio between the diffraction peak intensities for anatase at 2θ: 25.4° (101) and for WO₃ (220) at 2θ: 28.2°. It is worth highlighting that these changes

($I_{(220)} \text{WO}_3 / I_{(101)} \text{TiO}_2$) were correlated to the photocatalytic activity, observed during the photodegradation of MO and ASP. This correlation, as well as others, will be discussed in greater detail in Section 3.

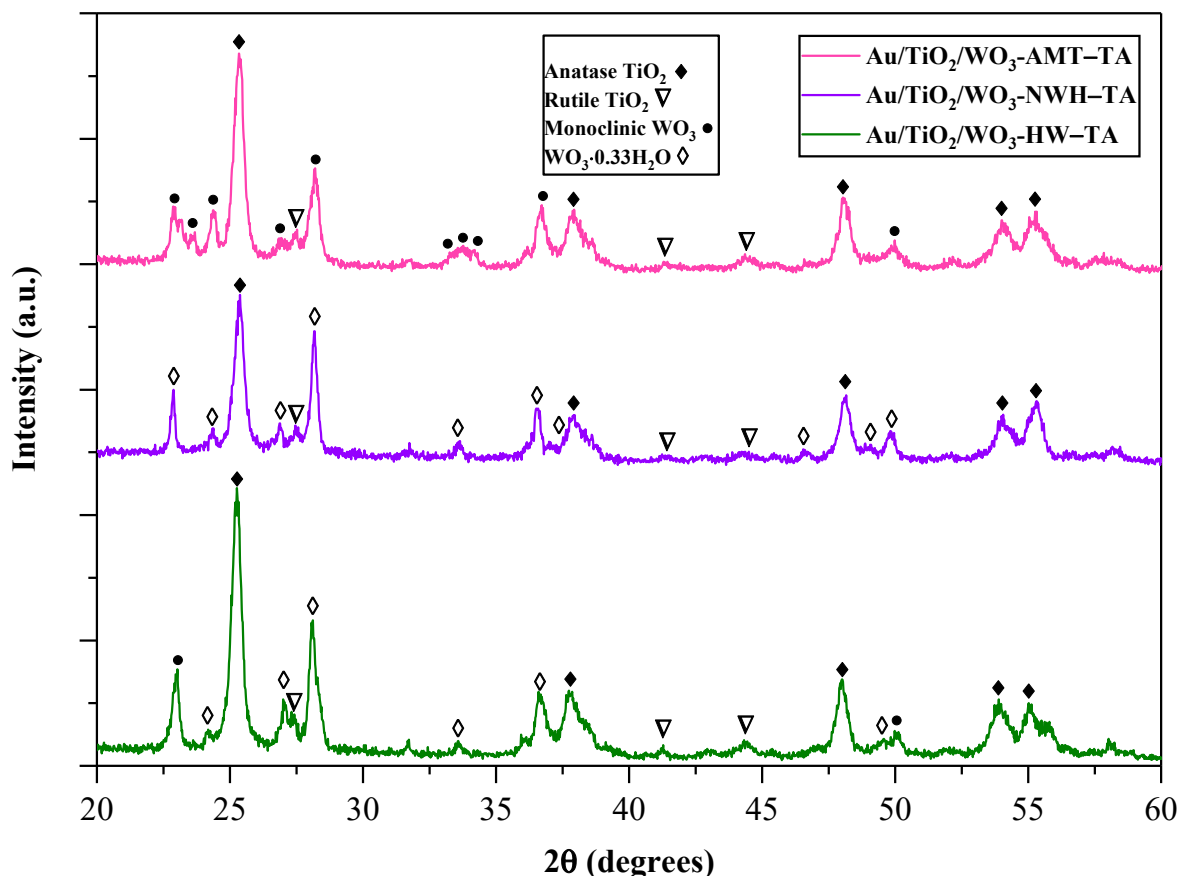


Figure 2. XRD patterns of the Au/TiO₂/WO₃ heterostructures obtained via the time-assisted method.

The deposition and formation mechanisms of Au NPs depend on the morphology, crystal structure, and crystal phase composition of the semiconductor [36–39]. Due to the non-covalent interaction between TiO₂ and Au NPs, the deposition of Au NPs is favored on the anatase crystal phase [40,41]. Commercial TiO₂'s anatase diffractions are located at 25.2° and 37.8°, whereas in the case of the Au/TiO₂/WO₃ heterostructures, these peaks are situated at 25.4° and 37.1°; thus, the slight shifts in the anatase peaks could be linked to the presence of Au NPs on anatase TiO₂. The probability that Au NPs are deposited on anatase TiO₂ is extremely high since the crystal phase composition of commercial TiO₂ is 89% anatase, and 11% rutile. This process can also be hindered or improved by introducing differently shaped and structured metal oxides, such as WO₃, into the composite system. This can result in TiO₂/WO₃ heterojunctions with improved photocatalytic activity under Vis light irradiation (compared with bare TiO₂).

In the case of the HA series, the XRD patterns of all crystal phases of the metal oxides can be identified without difficulties (Figure 1). However, in the case of the TA series (Figure 2), the identification of the crystalline phases proved to be difficult, due to modifications in the crystal structure of the composites. These modifications can be linked to the significantly longer synthesis duration of the Au reduction, and the presence of the trisodium citrate dihydrate in the suspension. The pH value of trisodium citrate dihydrate is between 7.5–9.0, whereas WO₃ and TiO₂ are highly stable in acidic environments. Above pH = 8, the WO₃ stability decreases due to the formation of sodium tungstate on the semiconductors' surface; thus, a local solubilization/desolubilization process occurs. Throughout the solubilization/desolubilization process, the W–O–H surface species pro-

gressively transform into W–O–Na species because the weakly acidic H⁺ from the W–O–H species is substituted by Na atoms, thus modifying the structure of the heterostructures. SEM–EDX spectra (Table 2) also confirmed a higher percentage of Na.

In the case of the hexagonal crystal phase (WO₃-NWH), the Au NP reduction method did not influence the WO₃ metal oxide lattice parameters (see Table 3); only a slight modification was observed for the c-axis (0.006 difference). In the cases in which WO₃ metal oxides had mixed crystal phases (WO₃-HW), according to the lattice parameters of the hexagonal and monoclinic crystalline phase, it can be argued that the unit cells are more dilated due to the presence of a higher percentage of water (and residual citrate). Regarding the Au NP HA reduction route, the a and b parameters of the hexagonal phase were slightly more dilated, whereas the c parameter was more dilated in the case of the TA route; concerning the monoclinic phase, the a and c lattice parameters were more dilated when the TA synthesis route was applied, and in the case of the HA synthesis route, the b parameters were dilated in a more significant manner. When solely monoclinic WO₃ metal oxides (WO₃-AMT) were added to the composite, the same behavior was observed as in the case of the WO₃-HW semiconductors: the a and c lattice parameters were more dilated when the TA synthesis route was applied. Regarding the HA synthesis route, the b parameter of the monoclinic phase was dilated more significantly. With the modification of the a, b, and c (hexagonal partial hydrate phase), respectively, the a, b, c and β (monoclinic phase) lattice parameters most probably were caused by their corresponding unit cell expansion, or by in certain cases, shrinking.

Table 3. Lattice parameters of the Au/TiO₂/WO₃ heterostructures.

Sample	Lattice Parameters						
	Hexagonal Partial Hydrate			Monoclinic			
	a	b	b	a	b	c	β
Au/TiO ₂ /WO ₃ -HW-HA	4.431	4.432	7.304	7.311	7.532	7.633	104.110
Au/TiO ₂ /WO ₃ -HW-TA	4.429	4.431	7.873	7.426	7.527	7.724	103.680
Au/TiO ₂ /WO ₃ -NWH-HA	4.416	4.416	7.738	-	-	-	-
Au/TiO ₂ /WO ₃ -NWH-TA	4.416	4.416	7.744	-	-	-	-
Au/TiO ₂ /WO ₃ -AMT-HA	-	-	-	7.297	7.527	7.610	105.060
Au/TiO ₂ /WO ₃ -AMT-TA	-	-	-	7.522	7.540	7.905	103.873

2.3. Optical Properties

The band gap values of the metal oxide components and their composites were also determined by employing the Tauc plot on the reflectance spectra of the samples and are presented in Table 4. The band gap values of the WO₃-HW, WO₃-NWH and WO₃-AMT are situated in the visible domain of the spectrum at 450 nm, 460 nm, and 550 nm, respectively. By adding 24 wt. % WO₃ to the commercial TiO₂, the band gap value of TiO₂ was only slightly modified: from 3.11 eV to 3.00 eV for TiO₂/WO₃-HW; from 3.11 eV to 2.97 eV for TiO₂/WO₃-NWH; and no modification was observed for TiO₂/WO₃-AMT, with a band gap of 3.10 eV. The TiO₂/WO₃ composites can be employed as photocatalysts under UV irradiation since their band gaps reside in the close UV range of the spectrum (417–398 nm).

Table 4. Band gap values of TiO₂ and WO₃ metal oxides, and their corresponding TiO₂/WO₃ composites [31].

Sample	TiO ₂	WO ₃ -HW	WO ₃ -NWH	WO ₃ -AMT	TiO ₂ /WO ₃ -HW	TiO ₂ /WO ₃ -NWH	TiO ₂ /WO ₃ -AMT
Band gap value (eV)	3.11	2.75	2.69	2.25	3.00	2.97	3.10

The presence of Au NPs is evidenced by the reflectance spectra of the HA and TA samples (Figure 3). The plasmonic band of the Au NPs was identified in the 540–565 nm

region [42]. The Tauc plot (Supplementary Figure S16) was used to determine the band gap values of the ternary composites (Table 5).

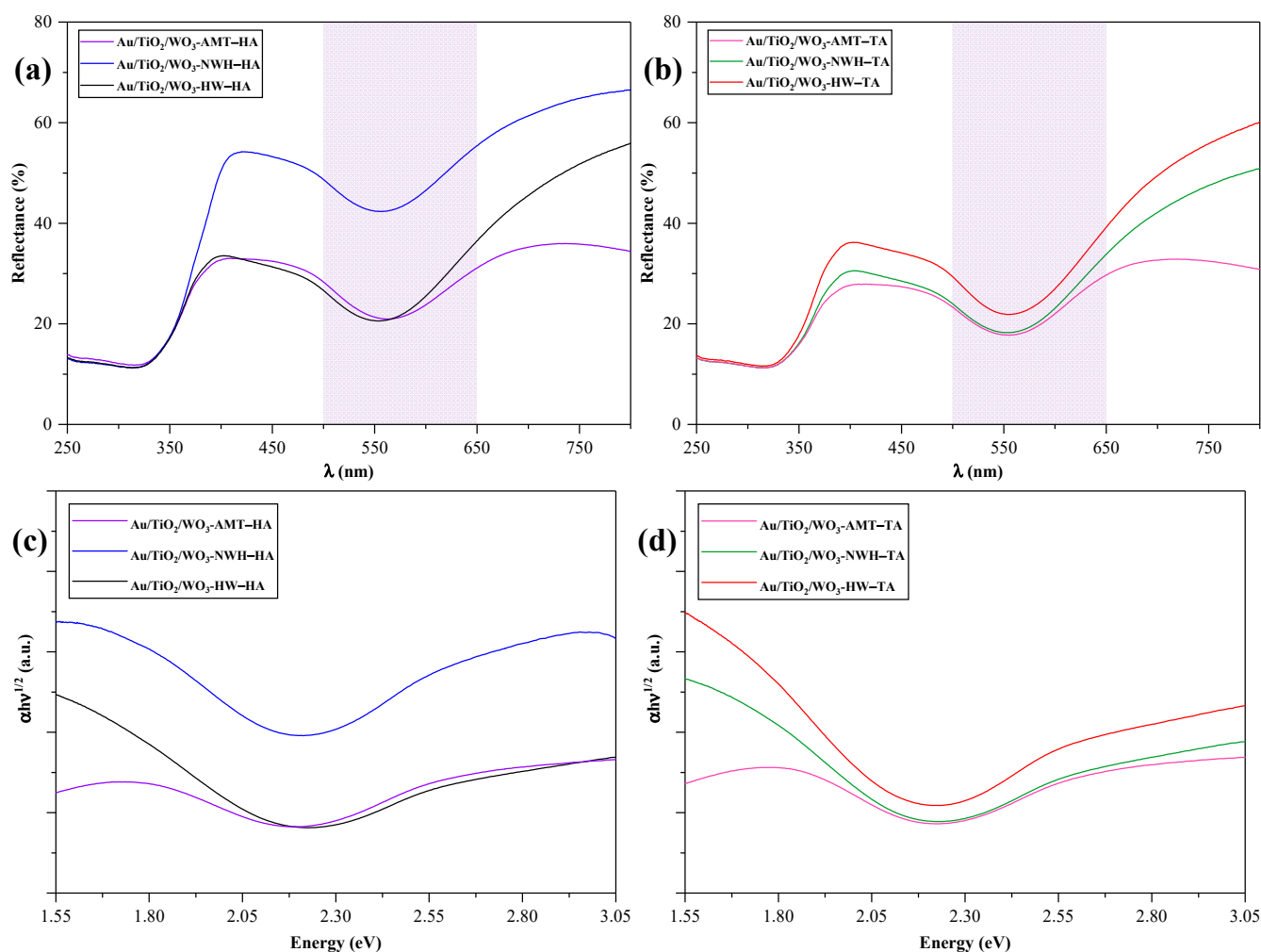


Figure 3. Diffuse reflectance spectra (a,b) and Tauc plots (c,d) of the Au/TiO₂/WO₃ heterostructures (Au NPs plasmonic band is highlighted in (a,b)).

Table 5. Band gap values of the ternary composites, determined from their corresponding Tauc plots.

Sample	Au/TiO ₂ /WO ₃ -HW-HA	Au/TiO ₂ /WO ₃ -HW-TA	Au/TiO ₂ /WO ₃ -NWH-HA	Au/TiO ₂ /WO ₃ -NWH-TA	Au/TiO ₂ /WO ₃ -AMT-HA	Au/TiO ₂ /WO ₃ -AMT-TA
Band gap value (eV)	2.25	2.23	2.60	2.24	2.32	2.22
Au wt. %	0.38	0.72	0.34	0.53	0.65	0.79

As we already mentioned, the TA synthesis route resulted in higher percentages of Au NPs in the Au/TiO₂/WO₃ heterostructures, leading to band gap values of ≈ 2.23 eV (≈ 555 nm) for each composite in the TA series. On the other hand, the HA synthesis route resulted in lower percentages of Au NPs (0.34, 0.38, and 0.65%). Only in the case of Au/TiO₂/WO₃-NWH-HA was a significant difference observed: 0.34% Au in the heterostructure led to a band gap value of 2.60 eV (≈ 477 nm), whereas in the case of a higher Au content, the band gap values were 2.25 eV (≈ 550 nm) and 2.32 eV (≈ 534 nm). The discrepancy in the Au/TiO₂/WO₃-NWH-HA band gap value is most probably due to the lower percentage of Au NPs in the heterostructure, as this was confirmed by XPS investigations also.

2.4. Raman Spectroscopy

Raman spectroscopy was employed to obtain a detailed insight into the TiO₂ and WO₃ metal oxide structures of the Au/TiO₂/WO₃ heterojunctions. By analyzing the Raman spectra of the samples (Figure 4), the TiO₂ and WO₃ characteristic vibrational modes were identified. Thus, the Raman bands corresponding to anatase TiO₂ vibrations were observed at 144 cm⁻¹ and 199 cm⁻¹, (symmetric stretching), at 396 cm⁻¹ (symmetric bending), and at 515 cm⁻¹ and 634 cm⁻¹ (anti-symmetric bending) [43,44]. Bands related to WO₃ vibrations were observed at 810 and 926 cm⁻¹, corresponding to the stretching vibrations of δ(W⁶⁺O) and the antisymmetric stretching vibrations of WO₂, respectively. The weak shoulder at ≈950 cm⁻¹ was attributed to the symmetric stretching vibration of W=O terminal bonds [45].

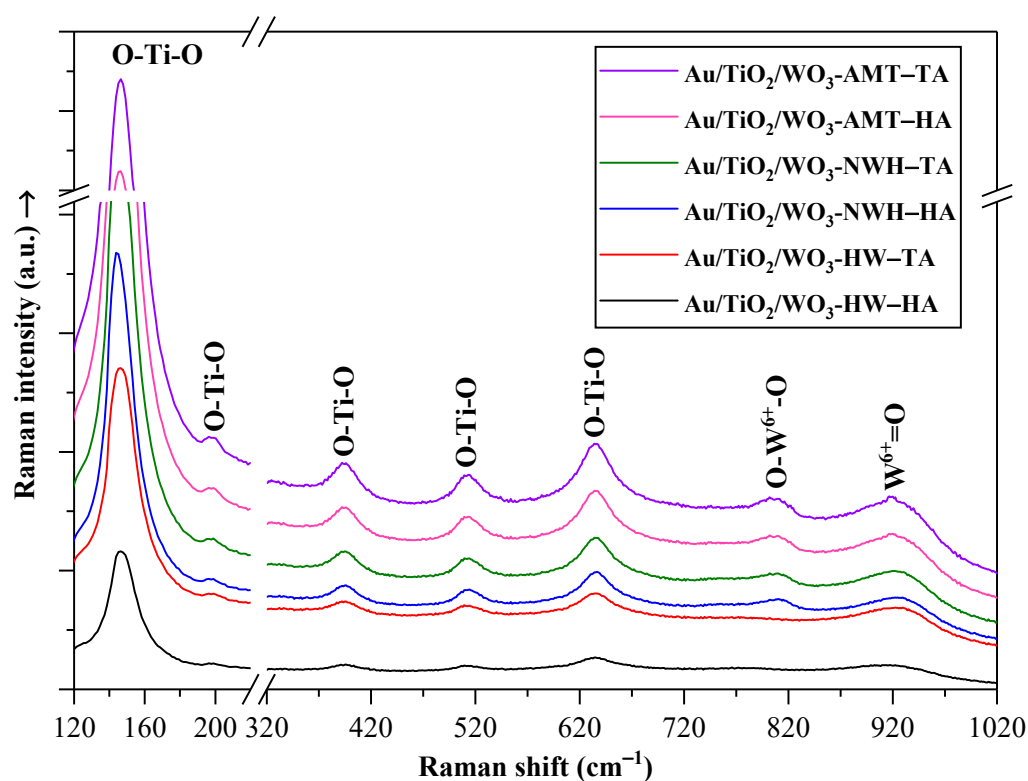


Figure 4. Raman spectra of the Au/TiO₂/WO₃ heterojunctions.

Changes in the ratio of the Raman bands specific to TiO₂ and hydrated WO₃ (Table 6) proved the structural and surface modifications (defects) that occurred in the heterostructures. These surface defects in the crystal lattice can act as traps for photogenerated charge carriers and influence the photocatalytic activity and selectivity of the samples [46]. These surface defects were most probably caused by the deposition of Au NPs. It was found that the TA Au reduction synthesis route led to an increased number of surface defects in WO₃ heterostructures containing either solely hydrated or mixed (monoclinic and hydrated) crystalline phases, whereas in the case of the solely monoclinic crystalline phase, the HA Au reduction led to slightly more surface defects.

Regarding the TiO₂ anatase ratio in the heterostructures, in the cases in which WO₃ solely hydrated or mixed crystalline phases were present (Au/TiO₂/WO₃-HW; Au/TiO₂/WO₃-AMT), the same trend was observed: TA Au reduction led to an increased number of surface defects, and the solely monoclinic crystalline phase led to slightly more surface defects when Au was reduced via the HA. This suggests that the composition of the crystalline phase not only plays an essential role in the mechanism of Au deposition, but also in the surface structure of the metal oxide.

Table 6. Intensity ratios of specific anatase TiO₂ and hydrated WO₃ Raman bands.

Sample	I ₅₁₅ /I ₃₉₆ (TiO ₂ Bands Ratio)	I ₈₁₀ /I ₉₂₆ (WO ₃ Bands Ratio)	WO ₃ Crystal Phases
Au/TiO ₂ /WO ₃ -HW-HA	0.919	0.952	Mixed
Au/TiO ₂ /WO ₃ -HW-TA	0.879	0.921	Mixed
Au/TiO ₂ /WO ₃ -NWH-HA	0.995	0.986	Hexagonal partial hydrate
Au/TiO ₂ /WO ₃ -NWH-TA	0.928	0.986	Hexagonal partial hydrate
Au/TiO ₂ /WO ₃ -AMT-HA	0.958	0.993	Monoclinic
Au/TiO ₂ /WO ₃ -AMT-TA	0.962	0.997	Monoclinic

When the crystalline phase of WO₃ was 100% hydrated (Au/TiO₂/WO₃-NWH), no difference was observed between the HA and TA Au reduction methods. Nevertheless, when the crystalline phase was mixed, the same trend was observed as that for TiO₂: the TA Au reduction synthesis route led to an increased number of surface defects. When the crystalline phase of WO₃ was 100% monoclinic (Au/TiO₂/WO₃-AMT), the same trend was observed as that for TiO₂: HA Au reduction led to an increased number of surface defects. However, it should be noted that for monoclinic WO₃, the ratio of I₈₁₀/I₉₂₆ was very close to an integer, which suggests that the number of surface defects formed was relatively low.

2.5. X-ray Photoelectron Spectroscopy (XPS)

XPS measurements were carried out to investigate the chemical composition of the heterojunctions. The XPS survey spectra of the Au/TiO₂/WO₃ heterojunctions proved the presence of each component in the composites. The TA synthesis route resulted in more Au NPs on the surface of the metal oxides than the HA synthesis route (Table 7), regardless of the WO₃ morphology or crystalline phase. The percentage of Au NPs was the highest for Au/TiO₂/WO₃-HW-TA and Au/TiO₂/WO₃-AMT-TA: 0.16% and 0.17%, respectively. These samples proved to be the most successful substrates for detecting crystal violet dye, as we will further show in one of the next paragraphs. The XPS survey spectra of the composites are presented in Figure 5.

Table 7. Chemical composition of the Au/TiO₂/WO₃ heterojunctions determined from the XPS spectra.

Sample	Atomic Composition (%)				
	O	C	Ti	W	Au
Au/TiO ₂ /WO ₃ -HW-HA	38.17	51.79	8.36	1.55	0.13
Au/TiO ₂ /WO ₃ -HW-TA	41.65	46.23	8.99	2.97	0.16
Au/TiO ₂ /WO ₃ -NWH-HA	35.07	54.07	9.84	0.95	0.07
Au/TiO ₂ /WO ₃ -NWH-TA	42.92	43.88	10.89	2.19	0.11
Au/TiO ₂ /WO ₃ -AMT-HA	33.59	57.77	7.34	1.23	0.07
Au/TiO ₂ /WO ₃ -AMT-TA	39.76	48.39	10.42	1.26	0.17

In the wide-scan spectra of the Au/TiO₂/WO₃ heterojunctions, W, Au, C, Ti, and O elements were identified as expected. The presence of WO₃ microcrystals was evidenced by the W 4f (Figure 6). W⁵⁺ (35.0 and 33.6 eV–4.5 at.%) and W⁶⁺ (34.8 and 37.0 eV–95.5 at.%) oxidation states were identified for WO₃ as being the representative species, while Ti 3p was considered as well during deconvolution [47–49]. The W 4d signal can reinforce the observations mentioned above [50,51]. The Ti 2p signal was attributed to the Ti 2p_{3/2} and Ti 2p_{1/2} Ti atom orbitals, respectively, to the Ti⁴⁺ oxidation state [52,53], while the presence of Ti³⁺ was not evidenced. The presence of the metallic Au NPs on the surface of TiO₂/WO₃ was evidenced by the Au 4f signal, and it was attributed to the presence of Au⁰ species [54,55]. Due to the low Au percentage (≤0.2 atomic %), the intensities of the Au 4f signals were weak. Neither the presence of Au⁺ nor Au³⁺ was identified in the samples.

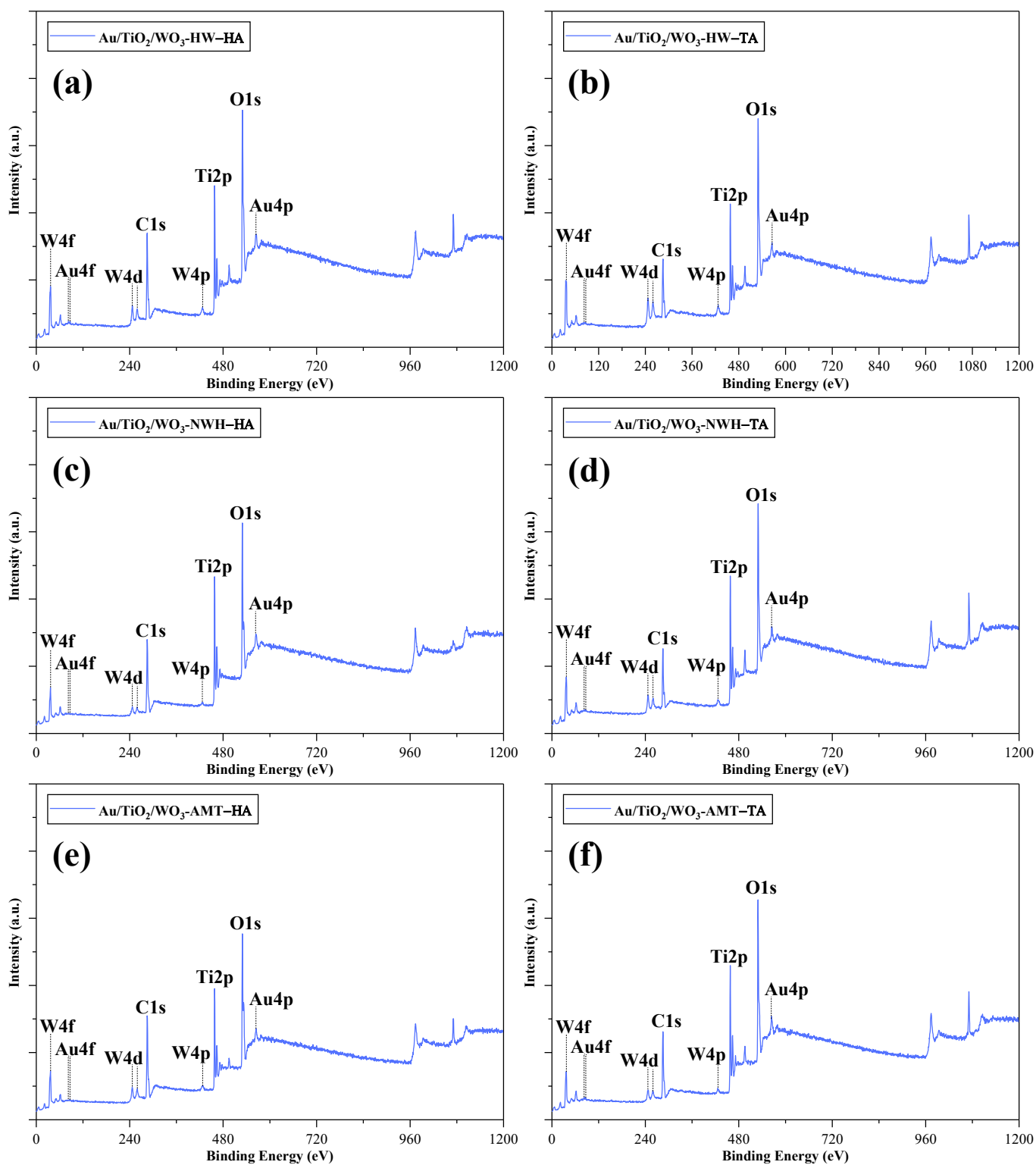


Figure 5. Individual XPS survey spectra of the Au/TiO₂/WO₃ heterostructures: (a) Au/TiO₂/WO₃-HW-HA; (b) Au/TiO₂/WO₃-HW-TA; (c) Au/TiO₂/WO₃-NWH-HA; (d) Au/TiO₂/WO₃-NWH-TA; (e) Au/TiO₂/WO₃-AMT-HA; and (f) Au/TiO₂/WO₃-AMT-TA.

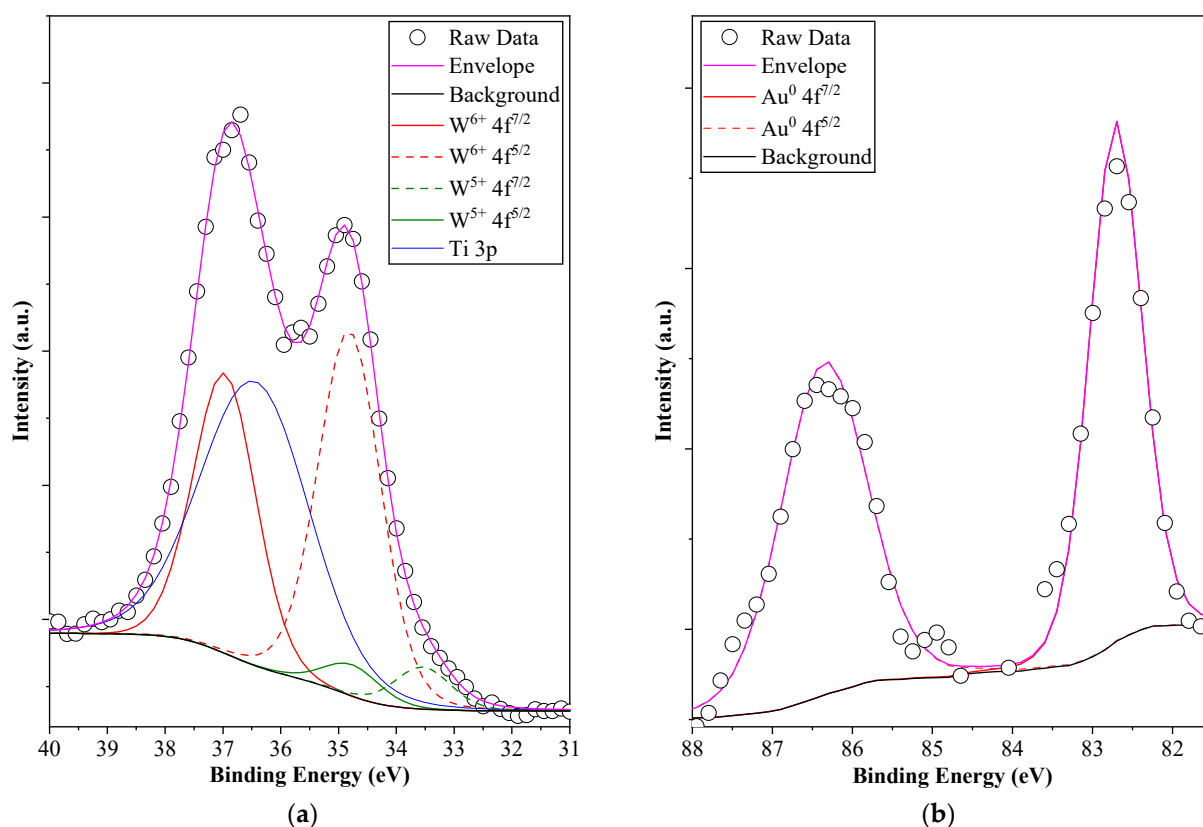


Figure 6. XPS spectra of the Au/TiO₂/WO₃-AMT-TA sample (W4f—(a) and Au4f—(b)).

XPS–VB spectroscopy was employed to determine the CB and VB edge values, and the results can be observed in Table 8. Based on the results, each Au/TiO₂/WO₃ heterojunction could enable the singlet electron reduction of the absorbed O₂ molecules to O₂^{•−} reactive oxygen species (ROS).

Table 8. Conduction and valence band alignments of the Au/TiO₂/WO₃ heterostructures.

Sample	eV		
	E _g	CB	VB
Au/TiO ₂ /WO ₃ -HW-HA	2.25	−0.56	1.69
Au/TiO ₂ /WO ₃ -HW-TA	2.23	−0.56	1.67
Au/TiO ₂ /WO ₃ -NWH-HA	2.60	−0.90	1.70
Au/TiO ₂ /WO ₃ -NWH-TA	2.24	−0.77	1.47
Au/TiO ₂ /WO ₃ -AMT-HA	2.32	−0.83	1.49
Au/TiO ₂ /WO ₃ -AMT-TA	2.22	−0.35	1.87

2.6. Photocatalytic Activity Assessment

Photocatalytic degradation tests were performed under UV light irradiation (2 h) for OA, PHE, and MO, while for ASP, Vis light irradiation (4 h) was used. OA (5 mM), PHE (0.5 mM) and MO (125 μM) removal were carried out under UV light irradiation because their concentration and stability were significantly greater than those of the ASP (50 μM) aqueous solution. The choice of the initial concentrations and the light source was based upon previous experience with photocatalytic tests for OA, PHE and MO [31,56–60]. For ASP, a lower concentration was chosen due to the limitations of the UV–Vis spectrophotometer, and a Vis light source was chosen because of the stability issues of ASP in general, and against UV light [61,62]. For commercial TiO₂, adsorption tests were carried out using each model pollutant, which was followed by the evaluation of photocatalytic activity (Figure S17). In

addition, for all model pollutants, photolysis experiments were carried out to assess their stability and eliminate the possibility of photodegradation in the photocatalysts absence.

After 2 h of UV light irradiation, photolysis yielded degradation rates of 6.0%, 1.0%, and 2.0% for OA, PHE, and MO, respectively. After 4 h of Vis light irradiation, photolysis resulted in a 2.9% degradation rate for ASP. After 2 h of adsorption on the surface of commercial TiO_2 , 0.0%, 0.9%, and 6.0% values were measured for OA, PHE, and MO, respectively. For ASP, this value was 1.9% after 4 h of adsorption. The $\approx 1\%$ photolysis yield in the case of the PHE model pollutant was due to the compound's high stability. The fairly low photolysis values for MO (2.0%) and ASP (2.9%) were attributed to their large molecular weight. The 6% photolysis for OA was attributed to its small molecular weight, contributing to its destabilization. Regarding photocatalytic conversions, values of 48.6%, 83.5%, 82.8%, and 73.1% were measured for OA, PHE, MO, and ASP, respectively.

Concerning the OA conversions, the most efficient heterostructures (Figure 7a and Table S1) were $\text{Au}/\text{TiO}_2/\text{WO}_3\text{-HW-TA}$ and $\text{Au}/\text{TiO}_2/\text{WO}_3\text{-NWH-HA}$, whereas the least efficient composite was $\text{Au}/\text{TiO}_2/\text{WO}_3\text{-AMT-HA}$. Except for $\text{Au}/\text{TiO}_2/\text{WO}_3\text{-AMT-HA}$, each sample had a higher photocatalytic activity than that of TiO_2 . For blade/plate-like and flower/sheet-like morphologies, the HA samples exhibited lower photocatalytic efficiencies (67.1% and 41.9%), whereas the TA samples showed higher photocatalytic activities (95.9% and 61.9%). The opposite behavior was observed for the rod/wire-like morphology (HA: 96.6% vs. TA: 62.6%).

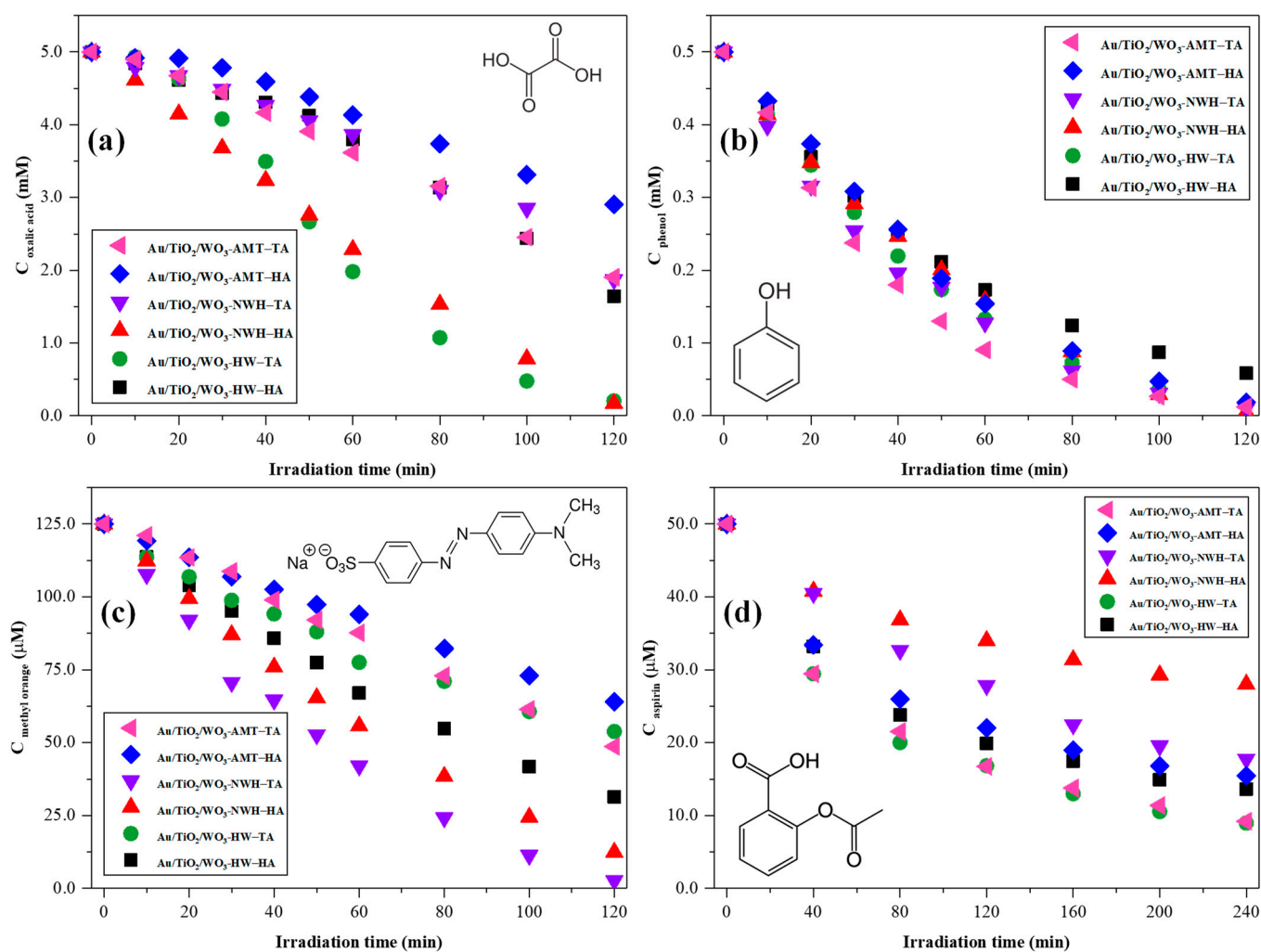


Figure 7. Photocatalytic activity of the $\text{Au}/\text{TiO}_2/\text{WO}_3$ heterostructures under UV light irradiation: (a) oxalic acid; (b) phenol; (c) methyl orange; and Vis light irradiation: (d) aspirin.

Regarding PHE photodegradation tests (Figure 7b and Table S1), every Au/TiO₂/WO₃ composite resulted in higher conversions than commercial TiO₂. Au/TiO₂/WO₃-AMT-TA and Au/TiO₂/WO₃-NWH-HA proved to be the most effective for PHE removal. The lowest photoactivity was observed for Au/TiO₂/WO₃-HW-HA, but even this composite proved more effective than commercial TiO₂ (88.3% vs. 83.5%). A similar result was obtained for PHE degradation as for OA degradation: the HA samples exhibited lower photoactivity for the blade/plate-like and flower/sheet-like morphologies (88.3% and 96.3%, respectively). At the same time, the TA samples exhibited higher photoactivity (96.8% and 98.2%, respectively), whereas for the rod/wire-like morphology, the opposite behavior was observed (HA: 99.0% vs. TA: 97.9%).

Concerning the MO photodegradation tests (Figure 7c and Table S1), it was observed that each composite could remove the dye with varying efficiencies. The most efficient heterostructures were Au/TiO₂/WO₃-NWH-HA and Au/TiO₂/WO₃-NWH-TA. Only these two composites yielded higher conversions than commercial TiO₂. Regarding the MO photodegradation tests, HA samples exhibited lower photocatalytic activity for rod/wire-like and flower/sheet-like morphology (90.1% and 48.8%, respectively), while TA samples exhibited increased photocatalytic activity (97.9% and 61.0%, respectively). The opposite behavior was observed for blade/plate-like morphology (HA: 74.9% vs. TA: 56.9%).

Concerning the photocatalytic degradation of ASP (Figure 7d and Table S1), the Au/TiO₂/WO₃-AMT-TA and Au/TiO₂/WO₃-HW-TA heterostructures proved the most efficient. Under Vis light irradiation, the following trend was observed: for all heterostructures, the HA samples had lower photoactivity (72.7%, 44.0%, 69.1%), whereas the TA samples had higher photoactivity (82.1%, 64.5%, 81.6%).

2.6.1. Photoluminescence (PL) of the Au/TiO₂/WO₃ Heterostructures

For the PL measurements, we selected the two Au/TiO₂/WO₃ heterojunctions that yielded the highest photocatalytic activity for most of the investigated pollutants (Au/TiO₂/WO₃-HW-TA and Au/TiO₂/WO₃-NWH-HA).

The PL spectra of commercial TiO₂ and the corresponding TiO₂/WO₃ heterostructures were also recorded for comparison purposes. The PL measurements were carried out at 365 nm excitation in the UV region and 450 nm in the Vis region. In the former case, the recombination rate of the photogenerated charge carriers (TiO₂) is inhibited if a metal oxide such as WO₃ is added to TiO₂. The recombination can be further inhibited by depositing Au NPs on the surface of TiO₂/WO₃ heterostructures. The increasing photocatalytic activity of the Au/TiO₂/WO₃ heterojunctions proves that the photogenerated charge carriers' recombination was successfully inhibited. Under UV-A light exposure (Figure 8a), the recombination of the Au/TiO₂/WO₃-HW-TA and Au/TiO₂/WO₃-NWH-HA heterojunction is nearly identical; the samples yielded similar photocatalytic removal efficiencies under UV light: 96.8 and 99.0% for PHE, respectively, and 95.9 and 96.6% for OA, respectively. The photocatalytic performance of TiO₂ was 83.5% for PHE and 48.6% for OA.

The PL spectra recorded in the visible region prove that the recombination of the TiO₂'s photogenerated charge carriers can be inhibited by coupling TiO₂ with another metal oxide (WO₃ in this case) and depositing Au NPs on its surface. Under Vis light exposure (Figure 8b), the inhibition of the recombination is low but observable, while for Au/TiO₂/WO₃-HW-TA, it was inhibited to a greater extent. In contrast, the inhibition was not as successful for Au/TiO₂/WO₃-NWH-HA; this was also observed in the photocatalytic removal efficiencies under Vis light: 82.1% and 44.0% for ASP, respectively. In comparison, TiO₂ degraded 73.1% of ASP.

2.6.2. Photocatalytic Recyclability and Stability of the Au/TiO₂/WO₃ Heterostructures

The stability and recyclability of the Au/TiO₂/WO₃ heterojunctions were studied for up to three photodegradation cycles for each model pollutant (Figure 9). The best-performing composites were chosen for recyclability assessment. Their stability was also assessed by recording the FT-IR spectra of the composites before and after photodegradation.

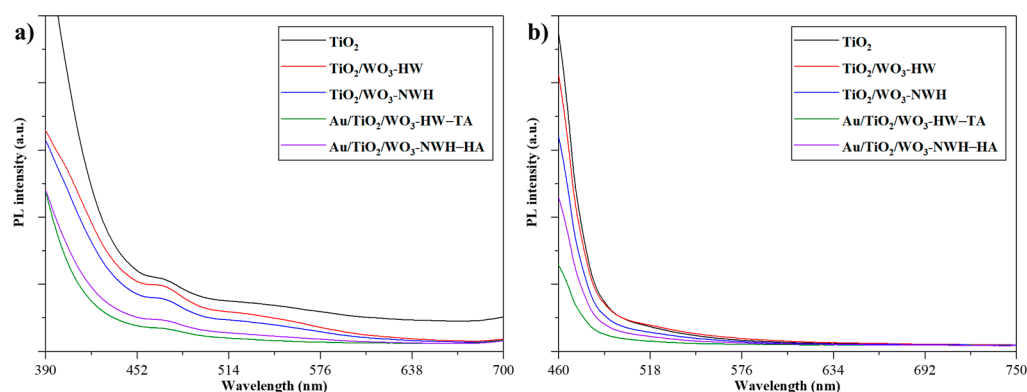


Figure 8. Photoluminescence spectra of commercial TiO₂, TiO₂/WO₃ heterostructures, and Au/TiO₂/WO₃ heterojunctions in the UV region (a) and Vis region (b).

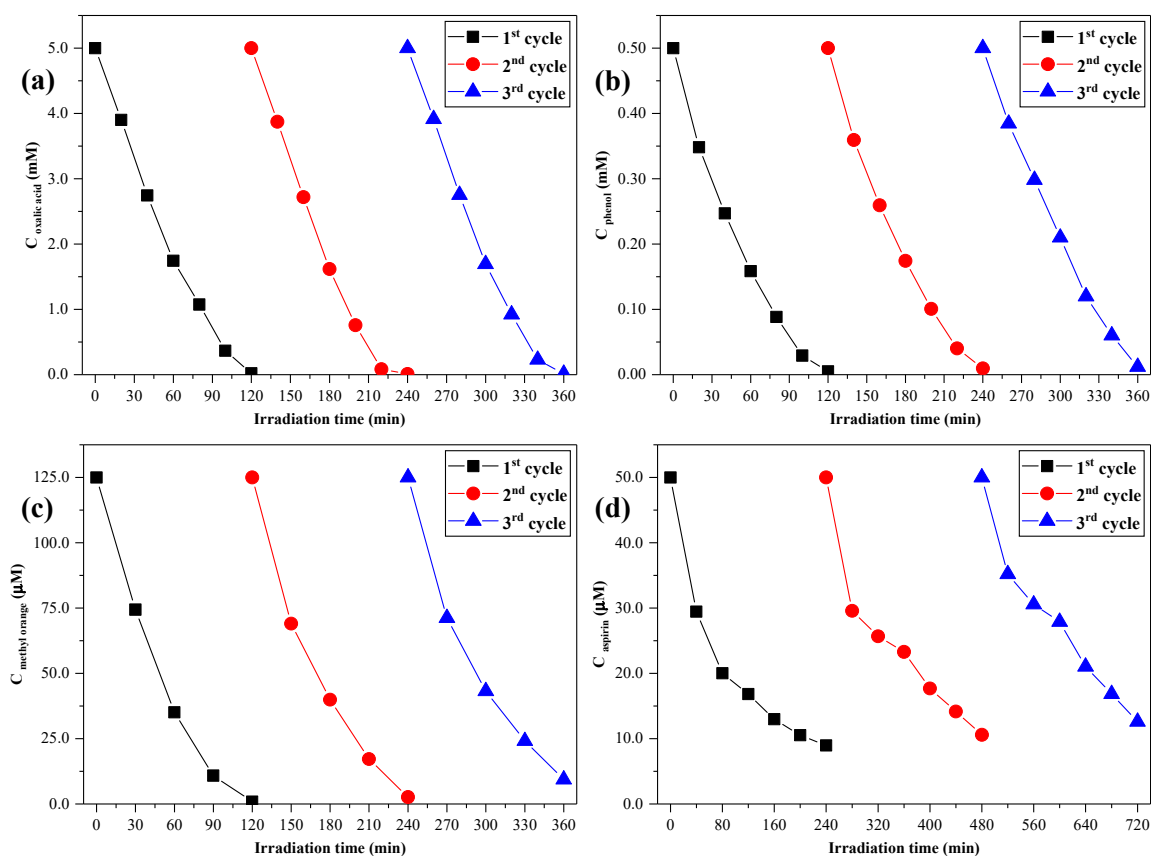


Figure 9. Recyclability of the Au/TiO₂/WO₃ heterojunctions in up to three photodegradation cycles: (a) OA photodegradation cycles, (b) PHE photodegradation cycles, (c) MO photodegradation cycles, and (d) ASP photodegradation cycles.

Au/TiO₂/WO₃-NWH–HA heterostructures were chosen to assess the recyclability and stability of the OA and PHE model pollutants. In the case of OA removal, the photocatalytic performance of the Au/TiO₂/WO₃-NWH–HA heterojunctions was almost identical in each cycle, yielding $\approx 99.0\%$ removal efficiency. In the case of PH removal, the photocatalytic performance decreased slightly after each cycle: from 99.0% to 98.1% and 97.6%. The difference between the conversion values after three cycles in the case of PHE removal was 1.4%. Au/TiO₂/WO₃-NWH–TA and Au/TiO₂/WO₃-HW–TA heterostructures were selected to determine the recyclability and stability of MO and ASP removal. The photocatalytic performance of the Au/TiO₂/WO₃-NWH–TA heterojunctions for MO removal decreased gradually but not drastically after each cycle: from 99.2% to 97.9%,

and 92.5% (6.7% difference). Concerning the photocatalytic activity of Au/TiO₂/WO₃-HW-TA for ASP removal, a decreasing trend was observed after each cycle, too, from 82.1% to 78.8% and 74.8% (7.3% difference). The Au/TiO₂/WO₃ heterostructures can successfully remove multiple pollutants, both under UV and Vis radiation exposure, for several utilization cycles.

The stability of the Au/TiO₂/WO₃ composites was assessed by recording the FT-IR (Figure S18) spectra prior to the photocatalytic degradation experiments and after each reusability cycle.

Thus, in the FT-IR spectra of the Au/TiO₂/WO₃-NWH-TA photocatalysts, prior to the OA and PHE photocatalytic removal (Figure S18a,b), the following absorption bands were identified: O-H stretching vibrations at $\approx 3420\text{ cm}^{-1}$ [59] (due to the presence of TiO₂ and WO₃ in the composite), H-O-H bending vibrations between 1640 and 1600 cm^{-1} [63], O-H bending vibrations at 1400 cm^{-1} [64], O-W-O stretching vibrations at 825 cm^{-1} ; and Ti-O-Ti and O-Ti-O stretching vibrations at 650 and 515 cm^{-1} [56]. According to the FT-IR spectra of the photocatalysts after three rounds of reutilization, no significant changes were observed: only in the case of the absorption bands related to adsorbed water molecules were minor modifications observed. The stability and recyclability of the photocatalysts in the case of OA and PHE photodegradation were proven by their high removal efficiency (OA: $\approx 99.0\%$; PHE: 97.6%) even after three cycles.

In the FT-IR spectra of the Au/TiO₂/WO₃-NWH-TA after the photocatalytic removal of MO (Figure S18c), the following absorption bands were observed: at $\approx 3400\text{ cm}^{-1}$, assigned to the O-H stretching vibration [59] (due to the presence of TiO₂ and WO₃); at 1636 cm^{-1} , attributed to the H-O-H bending vibration of the water adsorbed on the photocatalyst surface; at 1402 cm^{-1} , due to the O-H in-plane bending on the TiO₂ surface [64]; at 1129 cm^{-1} , assigned to the Ti-OH stretching vibration [65]; at 827 cm^{-1} , due to the O-W-O stretching vibration; and at 650 and 515 cm^{-1} , assigned to the Ti-O-Ti and O-Ti-O stretching vibrations, respectively [56]. After each reusability cycle, the FT-IR spectra of the photocatalyst did not change significantly. The changes observed for the bands at 1636 and 1402 cm^{-1} correspond to the adsorbed water on the surface of the photocatalysts, indicating that only marginal alterations occurred during the photoactivity experiments.

Regarding the stability of the Au/TiO₂/WO₃-HW-TA photocatalysts after the photocatalytic removal of ASP pharmaceuticals (Figure S18a), the following absorption bands were identified in the FT-IR spectra of the Au/TiO₂/WO₃-HW-TA heterojunctions: at $\approx 3460\text{ cm}^{-1}$, O-H stretching [66]; at 1636 cm^{-1} , H-O-H bending; at 1402 cm^{-1} , O-H in-plane bending on the TiO₂ surface [64] and W-OH bending [56]; at 958 cm^{-1} , W=O stretching [67]; at 815 cm^{-1} , O-W-O stretching [68]; and Ti-O-Ti and O-Ti-O stretching vibrations at 649 and 514 cm^{-1} [69,70].

In the case of ASP removal, the same trend was observed as in the case of the other pollutants (OA, PHE, and MO) from the FT-IR spectra: the reutilization of the photocatalysts did not induce structural modifications in the photocatalysts; only the intensities of the adsorbed water molecules increased slightly. The obtained Au/TiO₂/WO₃ heterojunctions for this study possess high stability, even after several reutilization cycles; their photocatalytic performance diminished by 7.3% (in the case of ASP removal) after three cycles, by 6.8% for MO removal, by 1.4% for PHE removal, and in the case of OA removal, the photocatalytic performance was almost identical.

The leakage of the metal ions from the Au/TiO₂/WO₃ heterostructures did not occur since Au NPs, TiO₂, and WO₃ are stable noble metals and metal oxides. Au NPs have great stability between pH = 5–9 and can be dissolved only with aqua regia. TiO₂ and WO₃ metal oxides are also stable in a wide pH range; WO₃ begins to decompose above pH = 10, and only HF and hot concentrated H₂SO₄ can dissolve TiO₂. The pH of the suspensions containing both the heterostructures and the model pollutant was $\approx \text{pH} = 5\text{--}6$; thus, the leakage of the metal ions is highly unlikely. The recyclability tests also confirmed this since the photocatalytic performance of the Au/TiO₂/WO₃ heterostructures did not decrease

drastically after three recycling steps; only a 7.3% decrease was observed in the case of MO removal (for OA, PHE, and ASP, this decrease was even less).

The VB positions of the heterojunctions were recorded by XPS measurements in order to understand the photocatalytic mechanism better. For this purpose, the heterojunctions with the highest photocatalytic activity under UV (Au/TiO₂/WO₃-NWH-HA) and Vis light (Au/TiO₂/WO₃-HW-TA) were chosen (Figures 10 and 11).

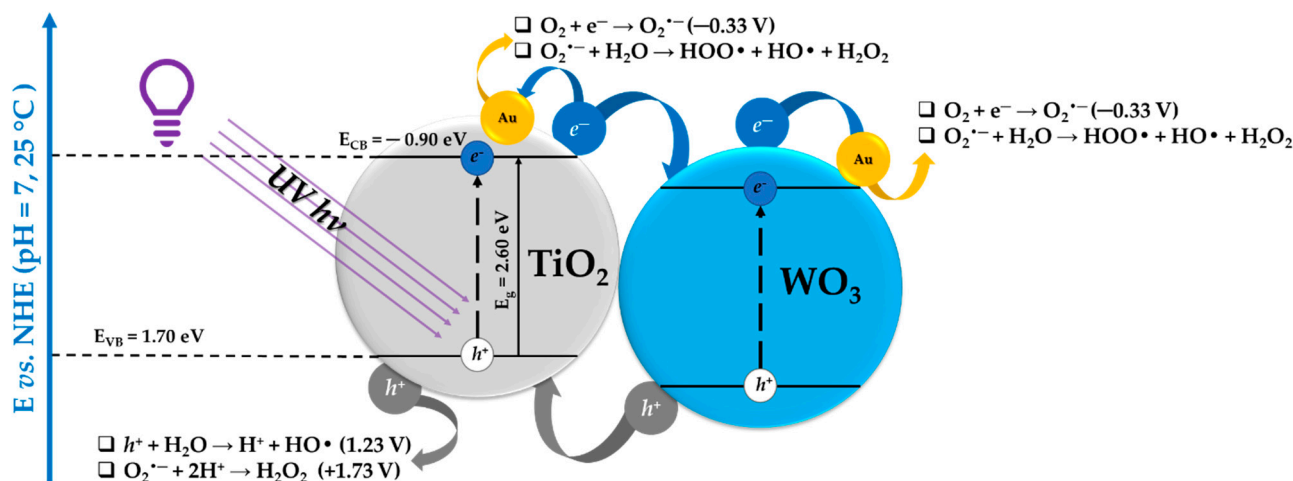


Figure 10. Proposed photocatalytic mechanism of the Au/TiO₂/WO₃ heterostructures under UV-A light exposure.

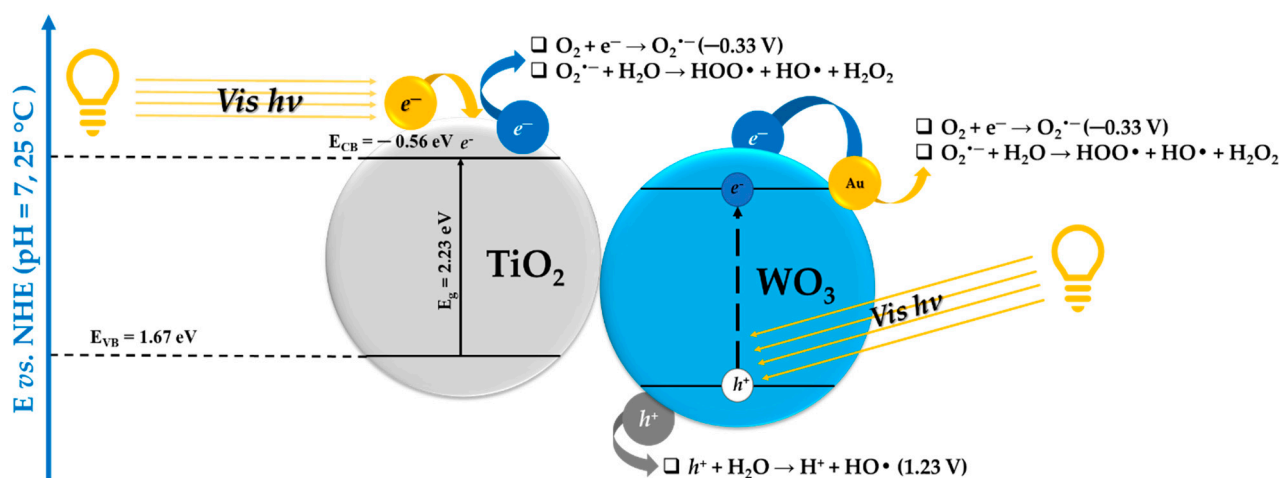
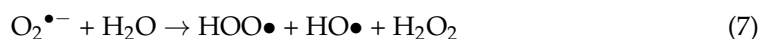
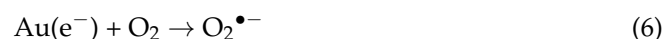
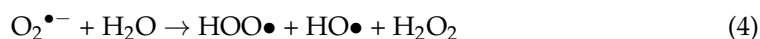


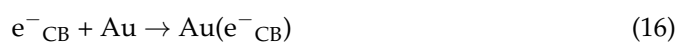
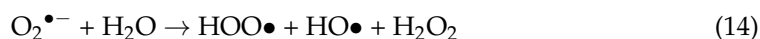
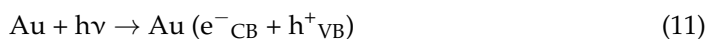
Figure 11. Proposed photocatalytic mechanism of the Au/TiO₂/WO₃ heterostructures under Vis light exposure.

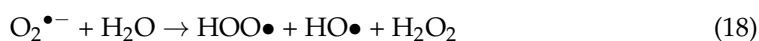
Upon the irradiation of the Au/TiO₂/WO₃ heterostructures with UV-A light (Figure 10), the photons are absorbed by the TiO₂ photocatalysts, followed by the charge separation of electrons and holes (e⁻, h⁺). The electrons migrate to the Au NPs located on the surface of the photocatalysts since Au acts as an electron acceptor. The redox potential of the O₂^{•-} is -0.33 V, and the CB position of the Au/TiO₂/WO₃ heterojunction is at -0.90 eV; hence, the formation of the superoxide radical anion is possible at the CB potential of the photocatalyst. The formation of other ROS, such as hydroperoxyl radical (HOO•), hydroxyl radical (HO•), or hydrogen peroxide (H₂O₂), is also possible due to the band alignment of the CB potential of the photocatalysts. The photogenerated electrons of TiO₂ can also migrate to the CB potential of WO₃, as WO₃ is also known to act as an electron acceptor. The electrons in the CB of WO₃ can further migrate to Au NPs, which leads to the formation of the aforementioned ROS. On the VB of the Au/TiO₂/WO₃ photocatalysts, WO₃ acts as

a donor of photogenerated holes since they migrate from WO_3 to TiO_2 . The VB potential of the sample is at 1.70 eV; thus, photogenerated holes can be utilized for water splitting, leading to the formation of $\text{OH}\bullet + \text{H}^+$. The generated $\text{O}_2^{\bullet-}$ can react with H^+ (formed during water splitting), producing H_2O_2 ROS.



When the Au/ TiO_2 / WO_3 composites are excited with Vis light (Figure 11), the photons are absorbed by the Au NPs and WO_3 . The photogenerated charge carriers from the Au CB migrate to the CB of TiO_2 . In this case, the CB potential alignment of the photocatalysts is at -0.56 eV; thus, the formation of $\text{O}_2^{\bullet-}$ is possible. Upon irradiation with Vis light, the Au NPs can act as electron donors and TiO_2 as electron acceptors, thus facilitating the single-electron reduction of the absorbed O_2 to $\text{O}_2^{\bullet-}$. Besides the formation of $\text{O}_2^{\bullet-}$ ROS, the formation of other species such as $\text{HOO}\bullet$, $\text{HO}\bullet$, or H_2O_2 is also possible on the CB potential of TiO_2 . Another pathway is also possible under Vis light irradiation: the photons are absorbed on the surface of WO_3 , followed by the photogeneration of electrons and holes. The electrons migrate to the CB of WO_3 ; in this case, WO_3 acts as the electron donor, whereas the Au NPs act as electron acceptors. The electrons from the CB potential of Au also assist in the formation of ROS such as $\text{O}_2^{\bullet-}$; $\text{HOO}\bullet$; $\text{HO}\bullet$ and H_2O_2 . Due to the VB potential alignment of the sample (1.67 eV), the photogenerated holes from the VB of WO_3 can be utilized for water splitting, leading to the formation of $\text{OH}\bullet + \text{H}^+$.





Regarding the photocatalytic mechanism of Au/TiO₂/WO₃ heterostructures, it can be argued that after the UV–A photoexcitation of the composites, the photogenerated charge carriers, more precisely the electrons (*e*[−]) from the TiO₂ CB, migrated to the Au NPs (migration caused by the formed Schottky barrier between TiO₂/WO₃ and Au NPs). Au NPs can act as reduction sites, while the adsorbed O₂ molecules on the surface of the composite can act as electron-trapping sites, thus enabling the formation of ROS such as O₂^{•−}; HOO•; HO• and H₂O₂. Au NPs can accept photogenerated electrons from TiO₂/WO₃, thus inhibiting the charge carriers' recombination, prolonging their lifetime and enhancing the photocatalytic performance. The photogenerated holes (h⁺) from the WO₃ VB can migrate to the VB of TiO₂, and they can participate in redox processes that will result in water splitting (•OH + H⁺). The generated •OH species and the oxidative holes (h⁺) can efficiently remove model pollutants via photocatalytic degradation. According to the formed intermediates, the photocatalytic experiments for PHE degradation prove that •OH species are generated in a higher volume than other ROS.

Concerning the ROS responsible for the photocatalytic degradation of the pollutants, in the case of OA removal, the photocatalytic photodegradation most likely occurred due to direct hole (h⁺) oxidation, since the photogenerated electrons reduced the W⁶⁺ species to W⁵⁺ of the WO₃ metal oxides, and this reduction led to the blue colorization of the suspension (Figure S19).

Regarding the ROS involved in the photocatalytic removal of PHE, it was concluded that •OH species were responsible. To prove this assumption, a chromatogram of the phenol degradation was added (Figure S20). According to the formed intermediates, the photocatalytic experiments for PHE degradation prove that •OH species are generated in a higher volume than any other ROS since the formed intermediates are hydroxylated forms of PHE (catechol, hydroxyquinol, resorcinol; and hydroquinone).

Concerning MO removal, the photocatalytic degradation of the azo dye can occur either by •OH or H₂O₂ species or by photogenerated holes. The photocatalytic mechanism depends on the MO concentration, due to the photocatalysts' ability to adsorb the dye [71,72]. In our case, MO was presumably decomposed in two main steps: the photogenerated holes broke the –N=N– azo bonds, and the •OH and H₂O₂ species decomposed the formed intermediates.

Regarding the ASP removal, since the photocatalytic degradation occurred under Vis light exposure, the photogenerated active species most likely were •OH and H₂O₂ species; thus, the photocatalytic degradation mechanism of aspirin likely yielded intermediates such as salicylic acid, PHE, gentisic acid, and hydroquinone. The likely intermediates hint that •OH was the ROS responsible for ASP removal [57].

2.7. Crystal Violet Dye Detection on Au/TiO₂/WO₃ Heterostructures Using SERS

The performance of Au/TiO₂/WO₃ heterostructures as SERS substrates was also evaluated. Crystal violet (CV) dye, a hazardous water pollutant, was chosen as the target molecule (C_{CV} = 10^{−6}–10^{−8} M). CV has a strong SERS activity, and its Raman cross-section is more well defined than that of other molecules [73,74]. CV was successfully detected on the Au/TiO₂/WO₃ substrates at concentrations as low as 10^{−6} M, 10^{−7} M, and 10^{−8} M. (Figures 12 and 13). The bands observed in the SERS spectra were attributed to the following vibrations: CH₃ torsion at 207 cm^{−1}, CNC bending at 439 cm^{−1}, C–N stretching at 725 cm^{−1}, CC_{center}C symmetric stretching and C–N stretching at 760 cm^{−1} [75], C–H bending at 801 cm^{−1} [76], CC_{center}C bending at 916 cm^{−1}, CC_{center}C asymmetric stretching at 1173 cm^{−1}, CC_{center}C asymmetric stretching and (CCC)_{ring}/C–H bending at 1296 cm^{−1} [75], C–N (N–phenyl) stretching at 1368 cm^{−1} [77], C–H bending, CH₃ sym-

metric bending, and $(CCC)_{\text{ring}}$ bending at 1387 cm^{-1} [78], and $C-C_{\text{ring}}$ stretching at 1445, 1475, and 1618 cm^{-1} [79–81]. The characteristic bands of CV dye could be observed in the SERS spectra recorded for each substrate. SERS bands with relatively strong intensities indicate the most probable interaction sites, which are the following: CH_3 (207 cm^{-1}), $C-C_{\text{ring}}$ (1618 cm^{-1}), $C-N$ and CCC_{ring} (1368 and 1387 cm^{-1} , respectively), central carbon atom (1173 cm^{-1}), $C-H$ (801 cm^{-1}), nitrogen atoms (439 cm^{-1}), and Π electrons in phenyl structures (1445 , 1475 , and 1618 cm^{-1}).

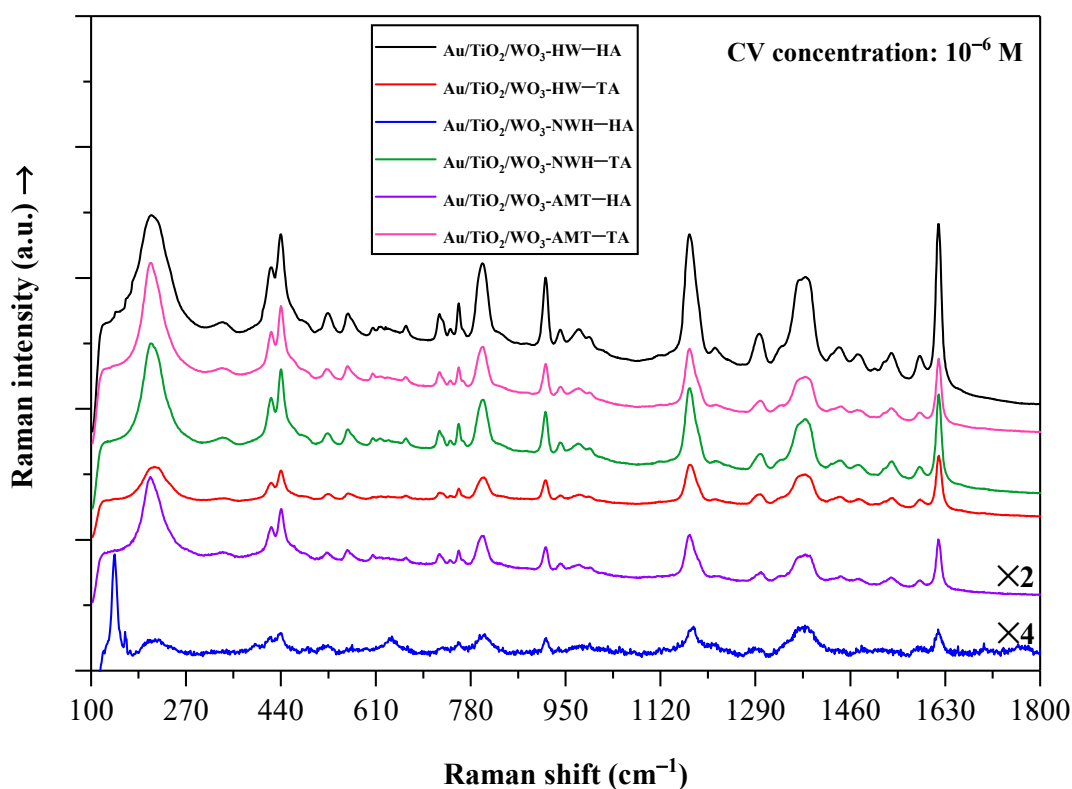


Figure 12. SERS spectra of crystal violet dye (10^{-6} M) adsorbed on various $\text{Au}/\text{TiO}_2/\text{WO}_3$ substrates.

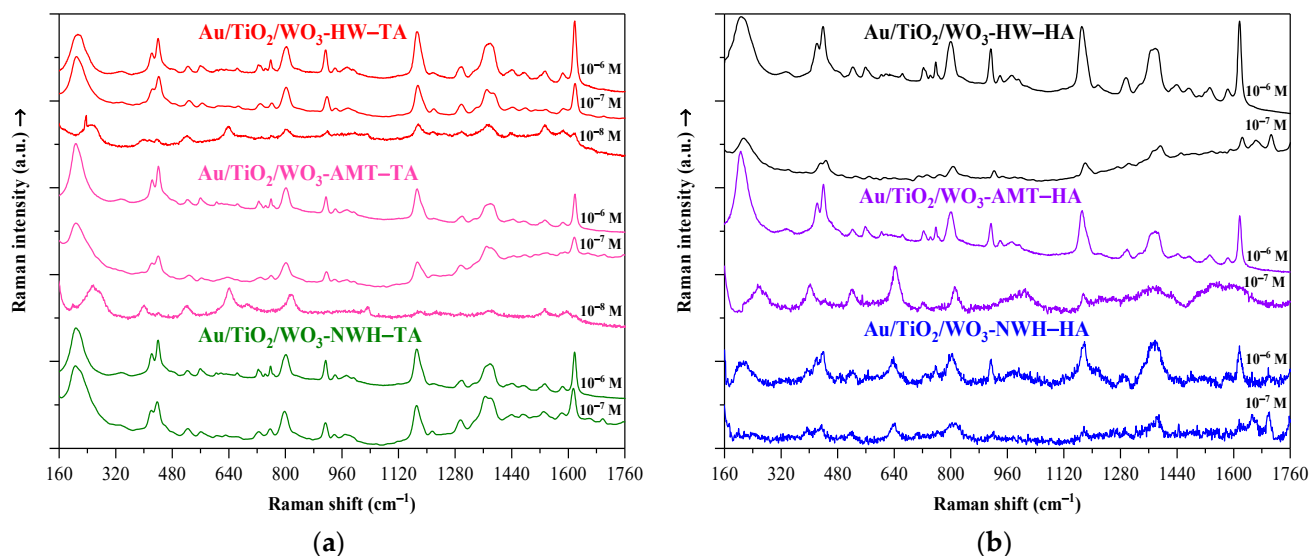


Figure 13. (a,b) Detection limit of crystal violet dye adsorbed on various $\text{Au}/\text{TiO}_2/\text{WO}_3$ substrates.

At lower CV concentrations (10^{-7} M), specifically in the case of the HA substrates in the 1650–1800 cm^{-1} region, other SERS bands were also observed. These bands (1654, 1699, and 1761 cm^{-1}) may imply the presence of amide bonds [82–84]. Amide bonds form via the condensation of carboxylic acids and amine functional groups, given that the carboxylic acid is activated at a high temperature or by a catalyst [85,86]. For the Au/TiO₂/WO₃ substrates from the HA series, the percentage of Au NPs was lower than that for the TA series, which resulted most probably in unreacted trisodium citrate dihydrate molecules. The formation of amide bonds could be possible (–CONH–) due to the interaction between trisodium citrate dihydrate ($\text{R}_1\text{-(CO)-O}^-\text{Na}^+$) and the quaternary amine functional ($\text{R}_2\text{-N}^+\text{vC}_2\text{H}_6$) groups of CV.

By analyzing the SERS spectra, it can be observed that some samples enhanced the Raman signal better than others. This difference can be linked to the morphology and size of Au NPs [87]. Regardless of the WO₃ morphology, the TA synthesis route resulted in more reduced Au NPs than the HA synthesis route. Higher Au NP percentages (TA series) provided greater SERS enhancement for each corresponding WO₃ morphology. It was found that larger amounts of Au NPs did not always result in higher SERS enhancement, indicating that WO₃ morphology could indirectly affect the SERS enhancement of the heterostructures.

At a CV concentration of 10^{-6} M (Figure 12), the best-performing heterostructure was Au/TiO₂/WO₃-HW-HA, whereas the SERS spectra obtained for the Au/TiO₂/WO₃-NWH-HA substrate had the lowest Raman band intensities. The relatively low enhancement performances of the Au/TiO₂/WO₃-NWH-HA substrate can be explained most likely by the low Au percentage of the sample (≈ 0.34 wt.%—SEM-EDX; 0.09%—XPS). Interestingly, the greatest Raman signal enhancements were not obtained for the Au/TiO₂/WO₃ heterostructures with the highest Au NPs contents.

At a lower CV concentration (10^{-7} M (Figure 13), the heterostructures' ability to detect the pollutant was reduced as expected, but the Au/TiO₂/WO₃-HW-TA, Au/TiO₂/WO₃-AMT-TA, Au/TiO₂/WO₃-NWH-TA, and Au/TiO₂/WO₃-HW-HA composites efficiently detected CV. In contrast, the Au/TiO₂/WO₃-AMT-HA and Au/TiO₂/WO₃-NWH-HA heterostructures most probably reached their detection limit for CV.

At a pollutant concentration of 10^{-8} M (Figure 13), it can be observed that only the Au/TiO₂/WO₃-HW-TA and Au/TiO₂/WO₃-AMT-TA substrates could detect CV. By comparing all the SERS spectra of CV on Au/TiO₂/WO₃ substrates, it can be concluded that the most promising heterostructures were Au/TiO₂/WO₃-HW-TA and Au/TiO₂/WO₃-AMT-TA, with a detection limit of 10^{-8} M (Table 9). By employing Au/TiO₂/WO₃ heterostructures with three differently shaped WO₃ metal oxides, meaningful insights can be obtained about the way morphology and structure indirectly influence the SERS-based sensorial capabilities of the Au/TiO₂/WO₃ heterostructures.

Table 9. Limit of detection (LoD) of the Au/TiO₂/WO₃ substrates for CV dye.

Sample	Limit of Detection (M)	Au wt. %	WO ₃ Crystal Phases
Au/TiO ₂ /WO ₃ -HW-HA	10^{-7}	0.38	Mixed
Au/TiO ₂ /WO ₃ -HW-TA	10^{-8}	0.72	Mixed
Au/TiO ₂ /WO ₃ -NWH-HA	10^{-7}	0.34	Hexagonal partial hydrate
Au/TiO ₂ /WO ₃ -NWH-TA	10^{-7}	0.53	Hexagonal partial hydrate
Au/TiO ₂ /WO ₃ -AMT-HA	10^{-7}	0.65	Monoclinic
Au/TiO ₂ /WO ₃ -AMT-TA	10^{-8}	0.79	Monoclinic

To assess the stability of the Au/TiO₂/WO₃ composites as SERS substrates, the best-performing ones were selected (Au/TiO₂/WO₃-HW-TA and Au/TiO₂/WO₃-AMT-TA), since according to the EDX and XPS investigations, these composites have the highest Au NP percentage, and both of them reached a detection limit of 10^{-8} M for CV dye.

Thus, the SERS spectra of the CV adsorbed on the Au/TiO₂/WO₃-HW-TA and Au/TiO₂/WO₃-AMT-TA in different concentrations (10⁻⁶–10⁻⁸ M) were recorded again after a considerably long period of time (4 years).

Even after such a long period, the Au/TiO₂/WO₃-HW-TA and Au/TiO₂/WO₃-AMT-TA heterojunctions were able to enhance the Raman signal of the CV dye, up to the nanomolar concentration (Figures 14 and 15). The new SERS spectra recorded by using the Au/TiO₂/WO₃-HW-TA substrates were more intense and well defined than those obtained when using the Au/TiO₂/WO₃-AMT-TA substrates; this was presumably caused by the higher adsorption affinity towards the CV molecules of the Au/TiO₂/WO₃-HW-TA. Thus, the strong intensity of the SERS spectra, together with the photocatalytic recycling tests, prove the extraordinary stability of the Au/TiO₂/WO₃ heterojunctions.

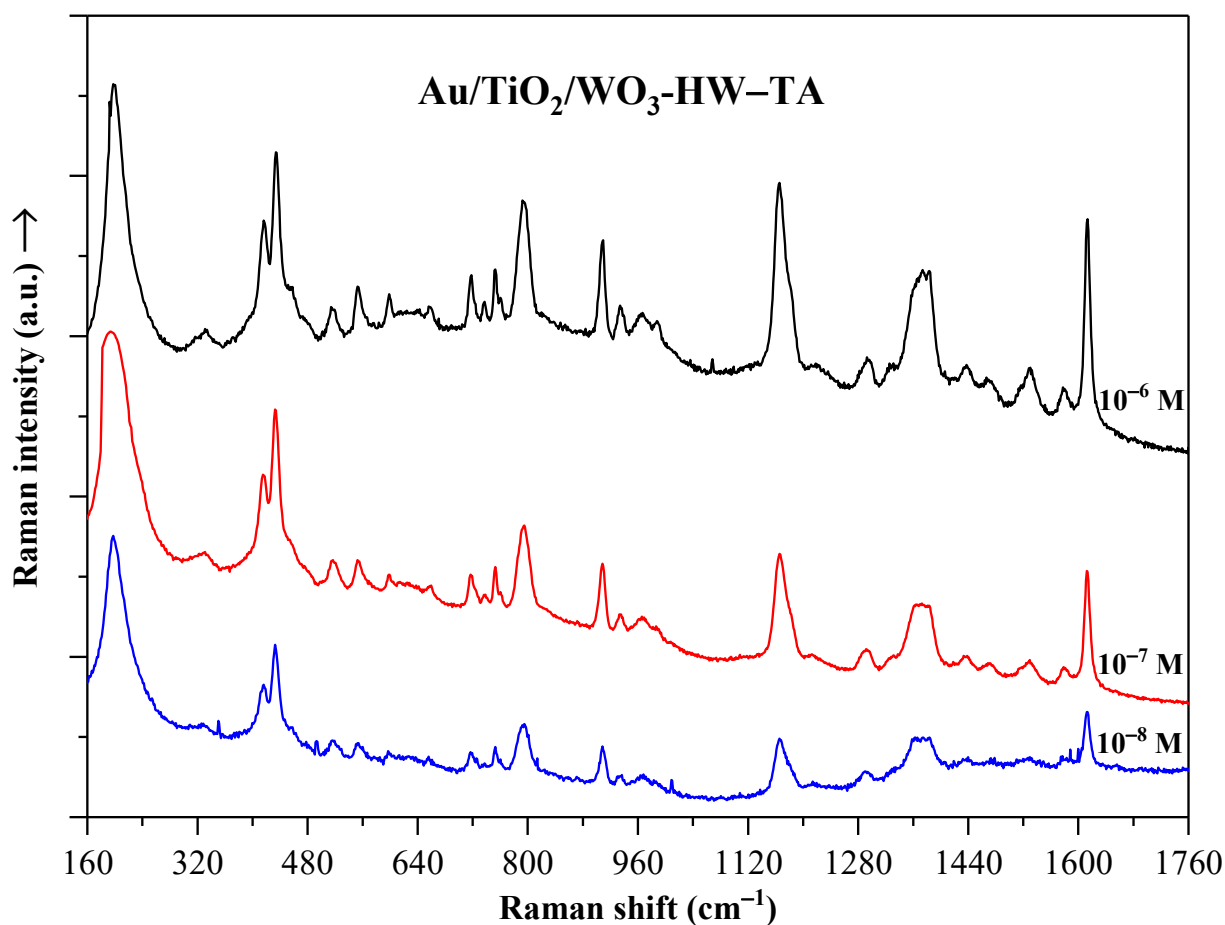


Figure 14. Newly recorded SERS spectra (after approx. 4 years) of crystal violet dye adsorbed on Au/TiO₂/WO₃-HW-TA substrates at different concentrations, as indicated.

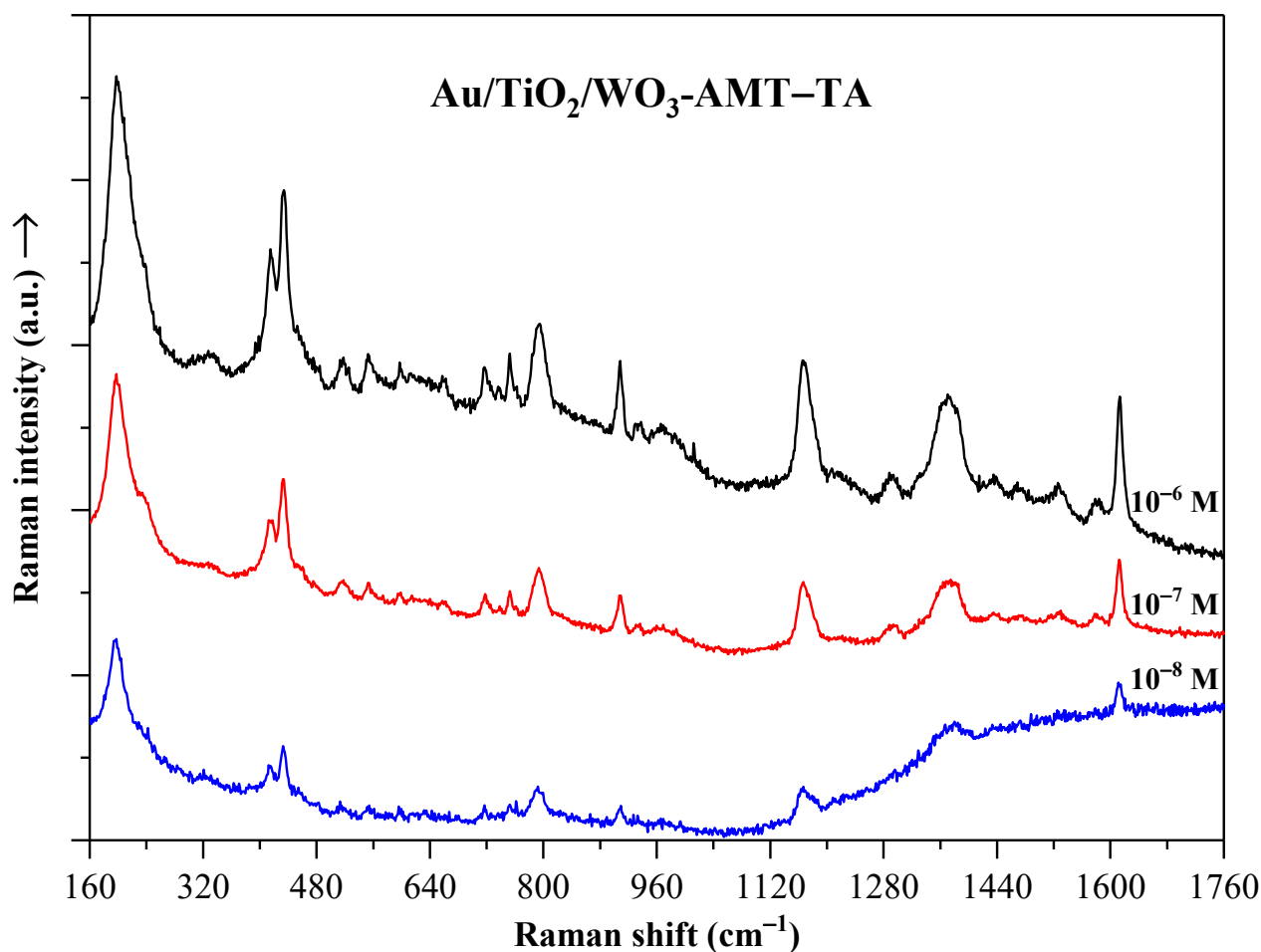


Figure 15. Newly recorded SERS spectra (after approx. 4 years) of crystal violet adsorbed on the Au/TiO₂/WO₃-AMT-TA substrates at different concentrations, as indicated.

3. Correlations between the Morpho-Structural Properties and Photocatalytic Activity of the Heterostructures

As discussed in Section 2.1., the size of the reduced Au NPs depends on the synthesis route and the morphology of the semiconductor. The TA synthesis route (Figure 16) resulted in slightly smaller Au NPs (19–21 nm). In contrast, the HA synthesis route led to somewhat larger Au NPs (21–24 nm), independent of WO₃ morphology. Concerning Au wt.% in the composites, we observed that the HA synthesis yielded a lower percentage (0.34, 0.38, and 0.65%), while the TA one yielded a higher percentage of Au (0.53, 0.72, and 0.79%). The amount of Au in the heterostructures depends on the tungsten oxide morphology and its crystal phase composition. The hexagonal partial hydrate crystal phase in both series led to a smaller Au NP size. In contrast, the monoclinic crystal phase led to a higher amount of deposited Au NPs.

The structural and optical properties of the Au/TiO₂/WO₃ heterostructures also depend on the method used to reduce Au (Figure 17). In the HA series, at a high WO₃(220)/TiO₂-A(101) ratio (0.92), when the relative surface defects of TiO₂ were barely noticeable (0.99), a blue shift was observed in the band gap (2.60 eV for Au/TiO₂/WO₃-NWH-HA); this blue shift was caused by the relatively small percentage of Au in the composite. In contrast, when the ratio of WO₃(220)/TiO₂-A(101) was lower (0.73 and 0.67) and the relative surface defects of TiO₂ were more accentuated (0.96 and 0.92), a red shift was observed in the band gap values (2.32 eV for Au/TiO₂/WO₃-AMT-HA and 2.25 eV for Au/TiO₂/WO₃-HW-HA). Regarding the TA series, the wt.% of the deposited Au (0.53, 0.72, and 0.79%) did not influence their band gap values; even at higher percentages,

the band gaps were nearly identical (≈ 2.2 eV). The plasmonic band maxima of the heterostructures obtained via the TA synthesis route were between 553–556 nm, indicating the presence of Au NPs [88,89].

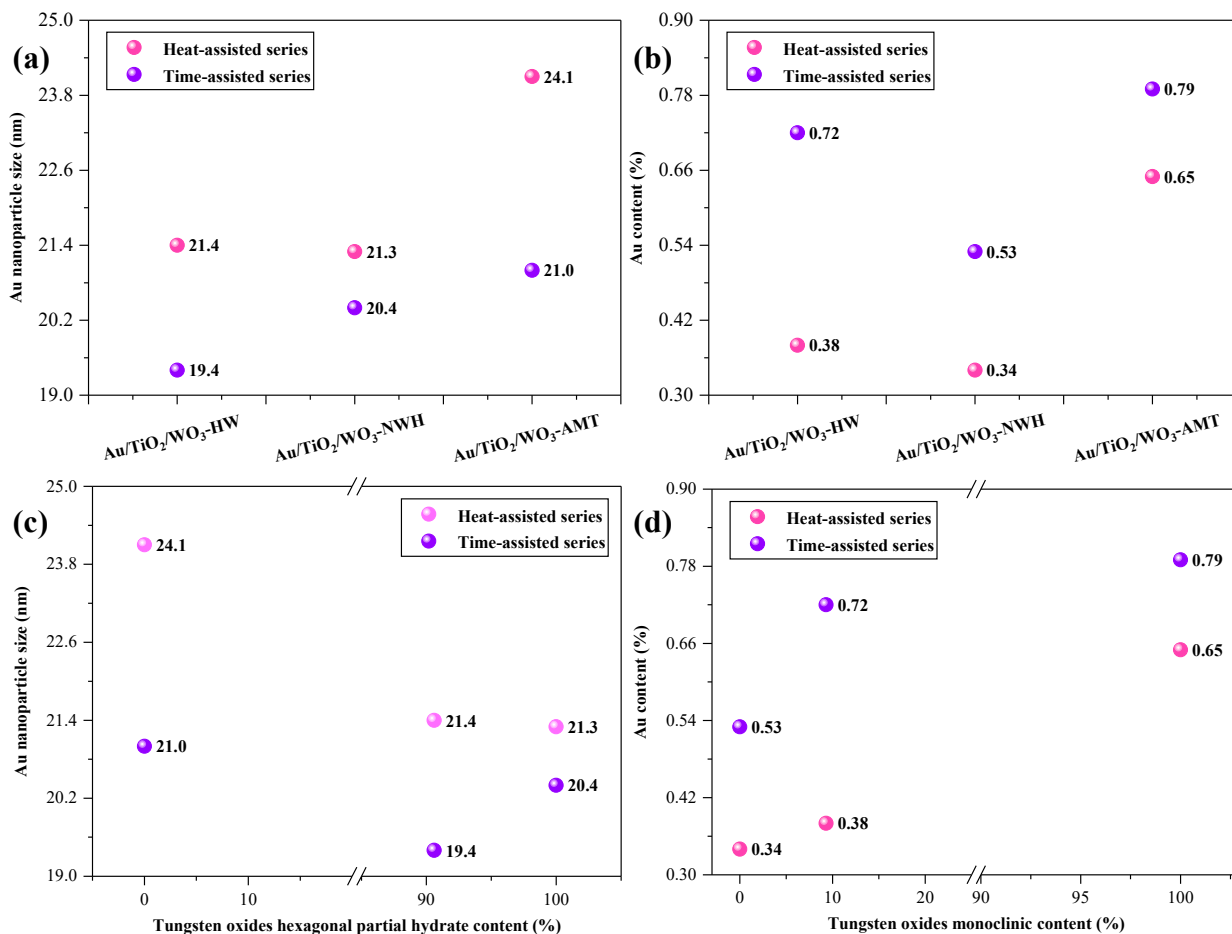


Figure 16. Correlations between the morpho-structural properties, Au reduction synthesis route, Au particle size, and Au wt.% of tungsten oxides in Au/TiO₂/WO₃ heterostructures: (a) Au NPs average size in function of Au deposition method and WO₃ morphology; (b) Au wt.% of the composites in function of Au deposition method and WO₃ morphology; (c) Au NPs average size in function of Au deposition method and HPH content in WO₃; and (d) Au wt.% of the composites in function of Au deposition method and MC content in WO₃.

The structural features of photocatalytic materials, such as the crystal phase composition, are paramount to defining their photocatalytic efficiency (Figure 17). It was observed that in the HA series, a high (90.6%) or solely (100%) hexagonal partial hydrate phase led to enhanced photocatalytic activity in MO (96.6%) and OA (90.1%) removal. However, when the crystal phase composition was purely (100%) monoclinic, the removal of MO (48.8%) and OA (41.9%) was significantly lower. Presumably, the hexagonal partial hydrate crystal phase and the rod-like morphology facilitate the generation of charge carriers (e^- , h^+) [90–92], inhibit their recombination, and prolong their lifetime; this was proven also by the PL measurements. This can result in enhanced photocatalytic efficiency for specific pollutants under UV light irradiation. TiO₂ surface defects also play a pivotal role in the photodegradation of ASP and PHE. The closer the I_{515}/I_{396} ratio of the TiO₂ Raman bands is to one, the lower the number of surface defects. In the HA series, more surface defects (0.92) proved beneficial for ASP removal (72.7%) under Vis light exposure. At the same time, for the removal of PHE (99.0%), a lower number of surface defects (0.99) proved to be more advantageous under UV light irradiation. Surface defects can influence the

degradation mechanism of a particular pollutant [56], since surface defects are related to the semiconductors' structure and morphology. In addition, the degradation mechanism depends on the irradiation source (UV or Vis) [93].

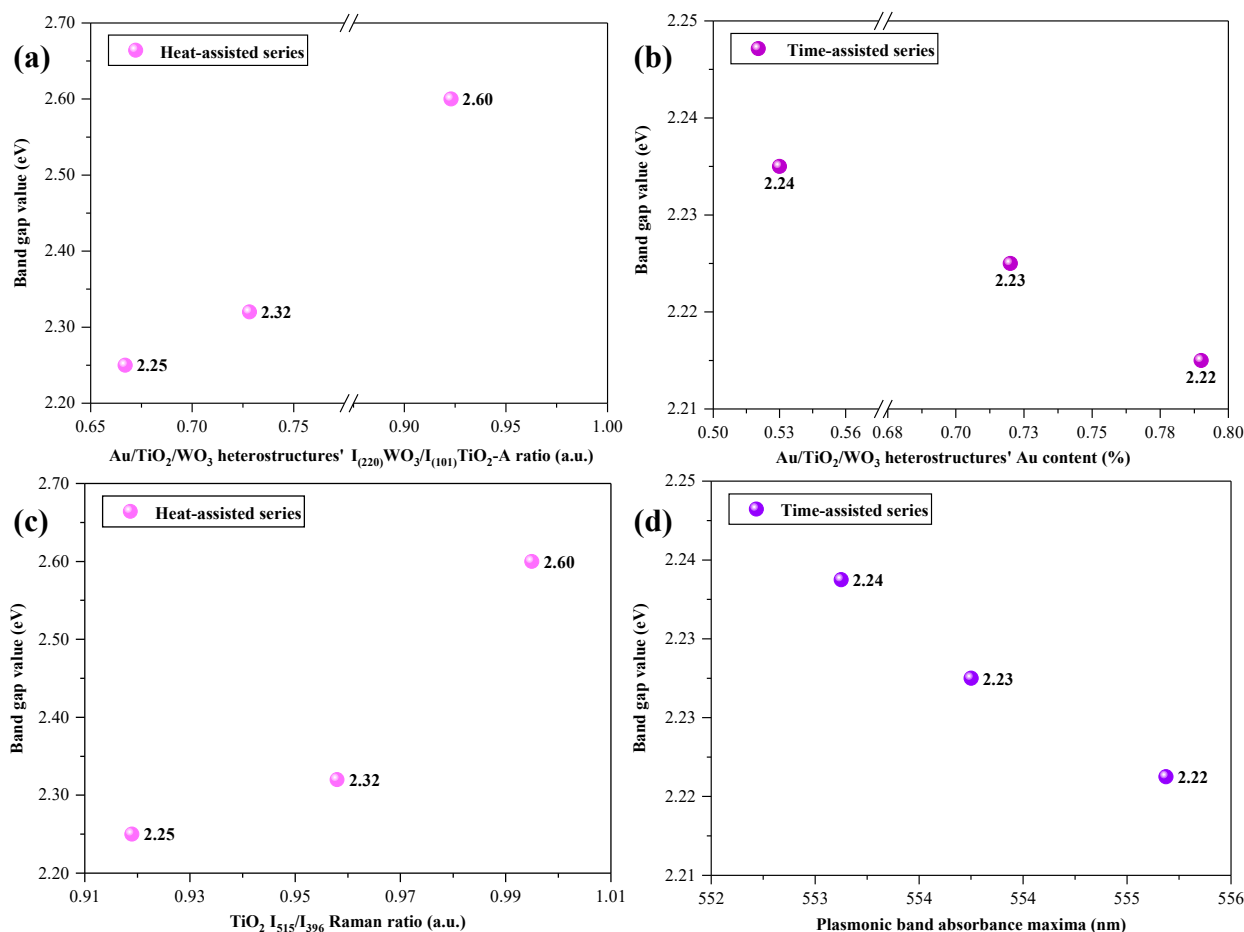


Figure 17. Correlations between Au reduction synthesis route, structural features, and the optical properties of Au/TiO₂/WO₃ heterostructures: (a) influence of WO₃(220)/TiO₂-A(101) ratio on the band gap energy values of heterostructures from the HA series; (b) Au wt.% influence on the band gap energy values of heterostructures from the TA series; (c) TiO₂ surface defects effect on the band gap energy values of heterostructures from the HA series, and (d) band gap energy values of the heterostructures from the TA series in function of the Au NPs plasmonic bands absorbance maxima.

As previously observed (Figure 17), the ratio of WO₃ and anatase TiO₂ facets can influence the band gap of Au/TiO₂/WO₃ heterostructures, and this could also affect their photocatalytic performance (Figure 18). Regarding the TA series, we found that lower WO₃(220)/TiO₂-A(101) ratios (0.52 and 0.84) led to enhanced photoactivity for ASP removal (82.1 and 81.6%) under Vis light. However, the photoactivity was reduced (64.5%) at a higher facet ratio (0.98). Interestingly, lower WO₃(220)/TiO₂-A(101) ratios (0.52 and 0.84) led to lower photocatalytic efficiencies (56.9 and 61.0%) for MO removal, while a higher facet ratio (0.98) enhanced the photoactivity (97.9%). The surface defects in TiO₂ also influenced the photocatalytic performance of the heterostructures obtained via the TA synthesis route. Concerning PHE removal, the same trend was observed for the TA series as for the HA series: fewer surface defects (0.96, 0.93, and 0.88) led to increased photocatalytic efficiency (98.2, 97.9, and 96.8%). Interestingly, when the removal of OA was studied, it was observed that a higher number of surface defects (0.88, 0.93, and 0.96) were more beneficial, resulting in higher conversions (95.9, 62.6, and 61.9%). Surface defects had the opposite effect on the photocatalytic efficiency of composites obtained via the TA

synthesis route for PHE and OA under UV irradiation. Most likely, more surface defects facilitate the formation of more h^+ rather than that of $\bullet OH$. It is well known that h^+ species favor the degradation of aliphatic compounds (such as OA or formic acid) in photocatalytic processes. The high number of surface defects in the TA series did not limit the formation of $\bullet OH$ significantly; thus, the photocatalytic activity of the composites was scarcely affected.

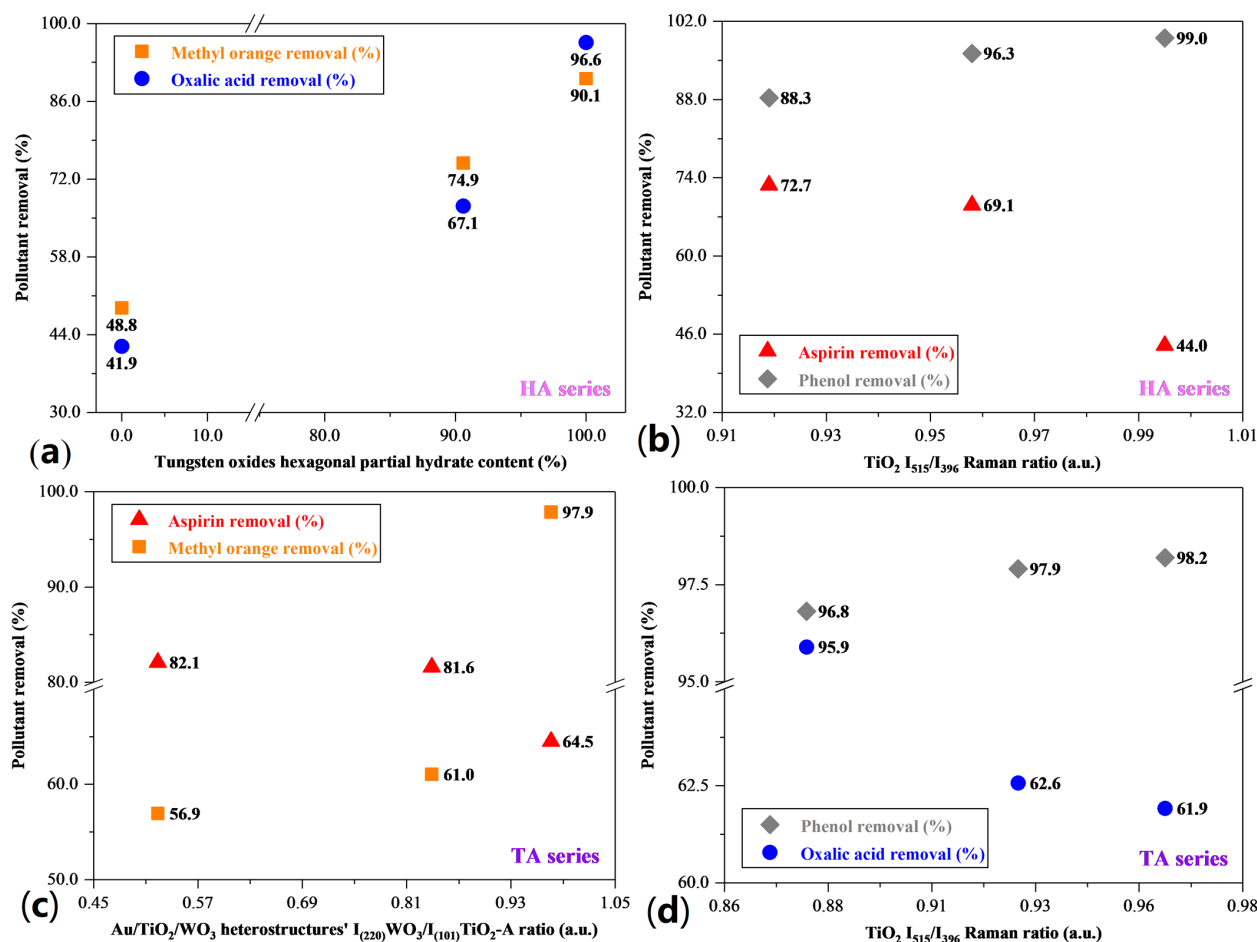


Figure 18. Correlations between the photocatalytic efficiency of Au/TiO₂/WO₃ heterostructures and their structural properties: (a) MO and OA removal efficiency in function of the tungsten oxides HPH percentage regarding the composites of HA series; (b) ASP and PHE removal efficiency in function of TiO₂ surface defects regarding the composites of HA series; (c) ASP and MO removal efficiency in function of WO₃(220)/TiO₂-A(101) ratio regarding the composites of TA series; and (d) PHE and OA removal efficiency in function of TiO₂ surface defects regarding the composites of TA series.

4. Materials and Methods

4.1. Chemicals

For the synthesis of WO₃ and WO₃·0.33H₂O, hydrogen peroxide (H₂O₂, 30%, Sigma Aldrich, Schnellendorf, Bavaria, Germany), tungstic acid (H₂WO₄, 99%, Sigma Aldrich, Schnellendorf, Bavaria, Germany), hydrochloric acid (HCl, 35–38%, 12 M, CHEM, Chemical Company, Iași, Romania), sodium tungstate dihydrate (Na₂WO₄·2H₂O, ≥99%, Sigma Aldrich, Schnellendorf, Bavaria, Germany), sodium chloride (NaCl, 99.5% CHEM, Chemical Company, Iași, Romania) and ammonium metatungstate hydrate ((NH₄)₆H₂W₁₂O₄₀·xH₂O, 99.99%, Sigma Aldrich, Schnellendorf, Bavaria, Germany) were used as received, without any further modifications. Deionized water (H₂O) was used as a solvent. The tungsten oxides obtained from tungstic acid will hereinafter be referred to as WO₃-HW; those from sodium tungstate dihydrate will be referred to as WO₃-NWH; and those from ammonium metatungstate hydrate will be referred to as WO₃-AMT.

To obtain the Au/TiO₂/WO₃ ternary composites, Aeroxide TiO₂ P25 ($\geq 99.5\%$, Evonik Industries, Essen, North Rhine-Westphalia, Germany), gold (III) chloride trihydrate (HAuCl₄·3H₂O, $\geq 99.9\%$ trace metal basis, Sigma Aldrich, Schnellendorf, Bavaria, Germany), trisodium citrate dihydrate (C₆H₉Na₃O₉, 99.0%, Chempur, Karlsruhe, Baden-Württemberg, Germany), and deionized water (H₂O) were used.

The photocatalytic activity of the composites was assessed via the photocatalytic degradation of 0.5 mM PHE (C₆H₅OH, Spektrum 3D, Debrecen, Hungary; analytical grade), 5 mM OA (C₂H₂O₄, $\geq 99\%$, Sigma Aldrich, Schnellendorf, Bavaria, Germany), and 125 μ M MO (C₁₄H₁₄N₃NaO₃S, 85%, Sigma Aldrich, Schnellendorf, Bavaria, Germany) aqueous solutions under UV light irradiation. In the same way, the photocatalytic efficiency of the composites was investigated under Vis light irradiation via the photocatalytic removal of 50 μ M ASP aqueous solution (tablets, C₉H₈O₄, 100 mg, 74%, Bayer, Leverkusen, North Rhine-Westphalia, Germany).

For recording the SERS spectra of CV dye (10^{-6} – 10^{-8} M) (ACS, C₂₅N₃H₃₀Cl, 90+%, Alfa Aesar, Tewksbury, MA, USA), water solutions were employed.

4.2. Synthesis Routes of the Au/TiO₂/WO₃ Ternary Composites

The Au/TiO₂/WO₃ ternary composites were prepared via the Turkevich–Frens chemical reduction pathway (HA: carried out at 90 °C for 4 h; and TA: carried out at 25 °C room temperature for 24 h), whereas the WO₃ and WO₃·0.33H₂O semiconductors were obtained via hydrothermal crystallization, according to these studies [31,58].

For the HA preparation of the Au/TiO₂/WO₃ composites, in each case, 750 mg of commercial TiO₂ was added to 48.78 mL of distilled water. Then, the suspension was stirred for 30 min, and 240 mg of WO₃ (or WO₃·0.33H₂O) was added, followed by another 30 min of stirring. The chemical reduction of Au NPs was ensured by the dropwise addition of 2 mL of 25.39 mM HAuCl₄ solution; then, the suspension was heated to 90 °C. After reaching the desired temperature, 5.08 mL of 38.8 mM C₆H₉Na₃O₉ was added to the suspension, followed by 60 min of stirring. In the final steps, the obtained suspensions were washed with distilled water and centrifuged, followed by drying (under air atmosphere) at 80 °C for 12 h. Three composites were obtained: Au/TiO₂/WO₃-HW–HA, Au/TiO₂/WO₃-NWH–HA, and Au/TiO₂/WO₃-AMT–HA.

Another series of Au/TiO₂/WO₃ composites were prepared via the TA synthesis route. In this case, 750 mg of commercial TiO₂ and 240 mg of WO₃ (or WO₃·0.33H₂O) were added to 48.78 mL of distilled water, then stirred for 30 min. In the next step, 2 mL of 25.39 mM HAuCl₄ solution was added dropwise to the suspension, followed by the immediate addition of 5.08 mL of 38.8 mM C₆H₉Na₃O₉ and 24 h of stirring. The as-obtained suspensions were washed and centrifuged with distilled water, then dried (under air atmosphere) at 80 °C for 12 h. Three composites were obtained: Au/TiO₂/WO₃-HW–TA, Au/TiO₂/WO₃-NWH–TA and Au/TiO₂/WO₃-AMT–TA.

4.3. Methods and Instrumentation and Assessment of Photocatalytic Activity

To probe the nano-scale assembly of the ternary composites, transmission electron microscopy (TEM) investigations were carried out using a FEI Tecnai F20 field emission high-resolution transmission electron microscope, operating at an accelerating voltage of 200 kV and equipped with an Eagle 4k CCD camera. The samples were dispersed in water and drop-casted on carbon-coated Formvar–Cu grids. The size distribution of the Au nanospheres was determined from the TEM images, where, in each case, at least 100 nanoparticles were considered. To prove the presence of the Au nanospheres, energy-dispersive X-ray (EDX) measurements were also carried out.

To investigate the morphology, scanning electron microscopy (SEM) measurements were performed using a Hitachi S-4700 Type II microscope (Japan, Tokyo) equipped with a cold field emission gun, at a 10 kV acceleration voltage. Micrographs were obtained by collecting secondary electrons using an Everhart–Thorney detector. EDX analysis was

performed with the same microscope using a Röntec XFlash Detector 3001 detector (Bruker, Karlsruhe, Germany).

X-ray diffraction (XRD) measurements were carried out on a Shimadzu XRD 600 diffractometer using a $\text{CuK}\alpha$ radiation source (1.54 Å) with a Ni filter. All diffractograms were recorded in the range of $20\text{--}50^\circ$ ($2\theta^\circ$), with a scanning speed of $2\theta^\circ \cdot \text{min}^{-1}$. The crystal phases of TiO_2 , WO_3 , and $\text{WO}_3 \cdot 0.33\text{H}_2\text{O}$ were identified using the JCPDS database.

Raman spectra were recorded using a confocal multi-laser Renishaw inVia Reflex spectrometer equipped with a RenCam CCD detector. During the measurements, the $\lambda = 532$ nm (green) laser line was employed as an excitation source with a power of 100 mW. A microscope objective with a NA of 0.9 at $100\times$ magnification was used to record the spectra in the $100\text{--}1100$ cm^{-1} domain. The integration time was 30 s for all Raman spectra, which were accumulated two times each. The ratios of the anatase TiO_2 and hydrated WO_3 Raman bands were calculated (I_{515}/I_{396} and I_{810}/I_{926}) to investigate the effect of surface modifications and the crystallinity of semiconductors in the composites.

The SERS spectra of the CV dye were obtained using the $\lambda = 633$ nm (red) laser line as an excitation source and a microscope objective with a NA of 0.35 at $20\times$ magnification in the range of $100\text{--}1800$ cm^{-1} . The integration time was 90 s for all spectra, without further accumulation cycles, using a laser power of 17 mW. The spectral resolution of the Raman and SERS spectra was 4 cm^{-1} . To prove the SERS stability of the substrates, the CV spectra at different concentrations (10^{-6} M– 10^{-8} M) were recorded after a long period of time (≈ 4 years) in similar conditions.

The diffuse reflectance spectra (DRS) of the samples were measured using a Jasco V650 spectrophotometer (Jasco, Vienna, Austria) equipped with an ILV-724 integration sphere. The spectra were recorded in the $250\text{--}800$ nm domain. The band gap values of the ternary composites were determined from the Tauc plot of the DR spectra.

The photoluminescence (PL) spectra of the $\text{Au}/\text{TiO}_2/\text{WO}_3$ heterostructures were acquired on a fluorescence spectrophotometer (Jasco LP-6500 spectrofluorometer, Jasco, Vienna, Austria) with a 1 nm spectral resolution equipped with a Xe lamp as the excitation source and coupled to an epifluorescence accessory (EFA 383 module). The measurements were recorded in the wavelength range of $350\text{--}800$ nm with fixed excitation wavelengths at 365 and 450 nm.

X-ray photoelectron spectroscopy (XPS) measurements were carried out with a SPECS Phoibos 150 MCD system (SPECS, Berlin, Germany) equipped with a monochromatic $\text{Al-K}\alpha$ source (1486.6 eV) at 14 kV and 20 mA, a hemispherical analyzer, and a charge neutralization device. The photocatalysts were fixed on a double-sided carbon tape that was completely covered by the sample. The binding energy scale was charged, according to the $\text{C}1s$, at 284.6 eV. High-resolution elemental spectra were obtained ($\text{W}4f$ and $\text{Au}4f$ shown in detail) using an analyzer in order to pass energy of 20 eV in steps of 0.05 eV for the analyzed samples. The data analysis was carried out using CasaXPS software (2.3.25 version). For the photocatalytic experiments that were carried out under UV light irradiation, fluorescent lamps (UV-A, $\lambda_{\text{max}} = 365$ nm) were used. For each photocatalytic test, the following parameters were applied: 2 h irradiation time, 6×6 W fluorescent lamps, 1 $\text{g}\cdot\text{L}^{-1}$ catalyst load, constant stirring (500 rpm), airflow, and temperature (25°C). The initial concentrations of the model pollutants were 125 μM , 5 mM, and 0.5 mM for MO, OA, and PHE, respectively. The photocatalytic efficiency of the ternary composites concerning OA and PHE removal was assessed using an Agilent 1100 high-performance liquid chromatograph (Agilent Technologies, Santa Clara, California, USA). For OA, the following conditions were used: 0.06% aqueous solution of sulfuric acid as the eluent, where the flow rate was 0.8 $\text{mL}\cdot\text{min}^{-1}$, a Grom Resin ZH column (Tankki Ltd., Ähtäri, Finland) as the stationary phase, and 206 nm as the detection wavelength. For phenol, the conditions were as follows: a mixture of methanol and water at a 1:1.857 ratio as the eluent, a BST Nucleosyl C-18 (4 mm \times 250 mm) column as the stationary phase, and 210 nm as the detection wavelength. A Jasco V650 spectrophotometer (Jasco, Vienna, Austria) was applied to investigate the removal of MO at a detection wavelength of 513 nm.

For the photocatalytic experiments that were carried out under Vis light irradiation, 6×6 W fluorescent lamps ($\lambda_{\min} \geq 400$ nm), 4 h irradiation, a $1 \text{ g}\cdot\text{L}^{-1}$ catalyst load, constant airflow, a constant temperature (25°C), and stirring (500 rpm) were used. The chosen model pollutant was ASP, and the initial concentration was $50 \mu\text{M}$. Employing a Jasco V650 spectrophotometer (Jasco, Vienna, Austria), we recorded the UV–Vis spectra of ASP between 190–400 nm to follow the removal efficiency. The ASP concentration was determined by integrating the area of the spectra after each measurement.

5. Conclusions

Multiple Au/TiO₂/WO₃ heterojunctions with enhanced photocatalytic efficiency towards multiple pollutants and SERS-based sensory/detection abilities (CV dye detection) have been successfully synthesized via two synthesis routes and by employing three different WO₃ morphologies. Au NPs were successfully deposited on the surface of TiO₂/WO₃ heterostructures regardless of the reduction method. The best-performing Au/TiO₂/WO₃ heterojunctions efficiently removed 96.6% of OA, 99.0% of PHE, and 97.9% of MO under UV light exposure, and 82.1% of ASP under Vis light irradiation. The stability and recyclability of the heterojunctions were confirmed after several reusability cycles as photocatalysts.

The Au/TiO₂/WO₃ heterostructures with the highest Au content (Au/TiO₂/WO₃-HW-TA; Au/TiO₂/WO₃-AMT-TA) were the best-performing SERS substrates, reaching a 10^{-8} M LoD for the CV dye. Au/TiO₂/WO₃ substrates proved to be highly stable, producing strong-intensity SERS signals even after a long period of time. The morphology, structure, and surface defects of WO₃ (and TiO₂) metal oxides are essential in the synthesis route of Au reduction on TiO₂/WO₃ heterostructures. By selecting the appropriate WO₃ morphology, crystal phase, and composition, Au/TiO₂/WO₃ heterojunctions with outstanding stability can be engineered to remove specific pollutants and to detect pollutants at concentrations close to the nanomolar range via SERS.

Supplementary Materials: The following supporting information can be downloaded at: <https://www.mdpi.com/article/10.3390/catal13061015/s1>, Figure S1: TEM micrographs of Au/TiO₂/WO₃-HW-HA (a) and Au/TiO₂/WO₃-HW-TA (b) samples, and their corresponding size distribution histograms for gold nanoparticles; Figure S2: TEM micrographs of Au/TiO₂/WO₃-NWH-HA (c) and Au/TiO₂/WO₃-NWH-TA (d), and their corresponding size distribution histograms for gold nanoparticles; Figure S3: TEM micrographs of Au/TiO₂/WO₃-AMT-HA (f) and Au/TiO₂/WO₃-AMT-TA (g), and their corresponding size distribution histograms for gold nanoparticles; Figure S4: SEM micrographs of the prismatic dipyrmaid WO₃-HW semiconductors (3–1 μm); Figure S5: SEM micrographs of the prismatic dipyrmaid WO₃-HW semiconductors (500–400 nm); Figure S6: SEM micrographs of the rod-like/wire-like WO₃-NWH semiconductors (3–2 μm); Figure S7: SEM micrographs of the rod-like/wire-like WO₃-NWH semiconductors (1–0.5 μm); Figure S8: SEM micrographs of the flower-like WO₃-AMT semiconductors (3–2 μm); Figure S9: SEM micrographs of the flower-like WO₃-AMT semiconductors (1–0.5 μm); Figure S10: SEM–EDX spectra of the Au/TiO₂/WO₃-HW-HA heterostructures; Figure S11: SEM–EDX spectra of the Au/TiO₂/WO₃-HW-TA heterostructures; Figure S12: SEM–EDX spectra of the Au/TiO₂/WO₃-NWH-HA heterostructures; Figure S13: SEM–EDX spectra of the Au/TiO₂/WO₃-NWH-TA heterostructures; Figure S14: SEM–EDX spectra of the Au/TiO₂/WO₃-AMT-HA heterostructures; Figure S15: SEM–EDX spectra of the Au/TiO₂/WO₃-AMT-TA heterostructures; Figure S16: Individual Tauc plots of the Au/TiO₂/WO₃ heterostructures: (a) Au/TiO₂/WO₃-HW-HA; (b) Au/TiO₂/WO₃-HW-TA; (c) Au/TiO₂/WO₃-NWH-HA; (d) Au/TiO₂/WO₃-NWH-TA, (e) Au/TiO₂/WO₃-AMT-HA; and (f) Au/TiO₂/WO₃-AMT-TA; Figure S17: Photolysis, adsorption, and photocatalytic activity measurements of commercial TiO₂ for each model pollutant: (a) oxalic acid; (b) phenol; (c) methyl orange; (d) aspirin; Figure S18: Stability of the Au/TiO₂/WO₃ heterostructures after several cycles of recyclability after OA removal (a); after PHE removal (b); after MO removal (c); and after ASP removal (d); Figure S19: Blue colorization of the OA suspension; Figure S20: Chromatograms of phenol at initial concentration and after 60 and 120 min of UV light exposure; Table S1: Summary of the Au/TiO₂/WO₃ heterostructures' photocatalytic activity under UV and Vis light irradiation.

Author Contributions: Conceptualization I.S., M.R. and T.G.; methodology I.S., Z.K., M.R. and T.G.; formal analysis M.B. and Z.P.; investigation I.S. and Z.K.; resources M.B. and Z.P.; writing—original draft preparation I.S.; writing—review and editing M.R., T.G., M.B. and Z.P.; visualization I.S. and Z.K.; investigation M.T. and M.F.; supervision M.B. and Z.P.; project administration M.B. and Z.P.; funding acquisition M.B. and Z.P. All authors have read and agreed to the published version of the manuscript.

Funding: This research was funded by the Executive Agency for Higher Education, Research, Development and Innovation Funding—UEFISCDI, project number PN-III-P1-1.1-TE-2019-1318, respectively PN-III-P1-1.1-TE-2019-1138. István Székely gratefully acknowledges the funding provided by the Hungarian Academy of Sciences “Domus Junior” scholarship.

Data Availability Statement: Data are contained within the article or supplementary material.

Conflicts of Interest: The authors declare no conflict of interest.

References

1. Rhaman, M.M.; Ganguli, S.; Bera, S.; Rawal, S.B.; Chakraborty, A.K. Visible-light responsive novel WO₃/TiO₂ and Au loaded WO₃/TiO₂ nanocomposite and wastewater remediation: Mechanistic inside and photocatalysis pathway. *J. Water Process Eng.* **2020**, *36*, 101256. [[CrossRef](#)]
2. Yang, X.; Fu, H.; Wang, W.; Xiong, S.; Han, D.; Deng, Z.; An, X. Enhanced solar light photocatalytic performance based on a novel Au-WO₃@TiO₂ ternary core-shell nanostructures. *Appl. Surf. Sci.* **2020**, *505*, 144631. [[CrossRef](#)]
3. Tahir, M.; Siraj, M.; Tahir, B.; Umer, M.; Alias, H.; Othman, N. Au-NPs embedded Z-scheme WO₃/TiO₂ nanocomposite for plasmon-assisted photocatalytic glycerol-water reforming towards enhanced H₂ evolution. *Appl. Surf. Sci.* **2020**, *503*, 144344. [[CrossRef](#)]
4. Zhu, Z.; Huang, W.R.; Chen, C.Y.; Wu, R.J. Preparation of Pd-Au/TiO₂-WO₃ to enhance photoreduction of CO₂ to CH₄ and CO. *J. CO₂ Util.* **2018**, *28*, 247–254. [[CrossRef](#)]
5. Karbalaee Akbari, M.; Hai, Z.; Wei, Z.; Detavernier, C.; Solano, E.; Verpoort, F.; Zhuiykov, S. ALD-Developed Plasmonic Two-Dimensional Au-WO₃-TiO₂ Heterojunction Architectonics for Design of Photovoltaic Devices. *ACS Appl. Mater. Interfaces* **2018**, *10*, 10304–10314. [[CrossRef](#)]
6. Zhang, B.; Yin, X.; Zhen, D.; Gu, W.; Liu, Y.; Cai, Q. Au nanoparticle-modified WO₃ nanoflowers/TiO₂ nanotubes used for the SERS detection of dyes. *New J. Chem.* **2017**, *41*, 13968–13973. [[CrossRef](#)]
7. Iliev, V.; Tomova, D.; Rakovsky, S.; Eliyas, A.; Puma, G.L. Enhancement of photocatalytic oxidation of oxalic acid by gold modified WO₃/TiO₂ photocatalysts under UV and visible light irradiation. *J. Mol. Catal. A Chem.* **2010**, *327*, 51–57. [[CrossRef](#)]
8. Karácsonyi, É.; Baia, L.; Dombi, A.; Danciu, V.; Mogyorósi, K.; Pop, L.C.; Kovács, G.; Coşoveanu, V.; Vulpoi, A.; Simon, S.; et al. The photocatalytic activity of TiO₂/WO₃/noble metal (Au or Pt) nanoarchitectures obtained by selective photodeposition. *Catal. Today* **2013**, *208*, 19–27. [[CrossRef](#)]
9. Kovács, G.; Baia, L.; Vulpoi, A.; Radu, T.; Karácsonyi, É.; Dombi, A.; Hernádi, K.; Danciu, V.; Simon, S.; Pap, Z. TiO₂/WO₃/Au nanoarchitectures' photocatalytic activity, “from degradation intermediates to catalysts' structural peculiarities”, Part I: Aerioxide P25 based composites. *Appl. Catal. B Environ.* **2014**, *147*, 508–517. [[CrossRef](#)]
10. Baia, L.; Vulpoi, A.; Radu, T.; Karácsonyi, É.; Dombi, A.; Hernádi, K.; Danciu, V.; Simon, S.; Norén, K.; Canton, S.E.; et al. TiO₂/WO₃/Au nanoarchitectures' photocatalytic activity “from degradation intermediates to catalysts' structural peculiarities” Part II: Aerogel based composites—Fine details by spectroscopic means. *Appl. Catal. B Environ.* **2014**, *148–149*, 589–600. [[CrossRef](#)]
11. Turkevich, J.; Stevenson, P.C.; Hillier, J. A study of the nucleation and growth processes in the synthesis of colloidal gold. *Discuss. Faraday Soc.* **1951**, *11*, 55–75. [[CrossRef](#)]
12. Frens, G. Controlled Nucleation for the Regulation of the Particle Size in Monodisperse Gold Suspensions. *Nat. Phys. Sci.* **1973**, *241*, 20–22. [[CrossRef](#)]
13. Rusu, M.; Baia, M.; Pap, Z.; Danciu, V.; Baia, L. Structural investigations of TiO₂-WO₃-Au porous composites. *J. Mol. Struct.* **2014**, *1073*, 150–156. [[CrossRef](#)]
14. Lu, X.; Dandapat, A.; Huang, Y.; Zhang, L.; Rong, Y.; Dai, L.; Sasson, Y.; Zhang, J.; Chen, T. Tris base assisted synthesis of monodispersed citrate-capped gold nanospheres with tunable size. *RSC Adv.* **2016**, *6*, 60916–60921. [[CrossRef](#)]
15. Sotnikov, D.V.; Berlina, A.N.; Ivanov, V.S.; Zherdev, A.V.; Dzantiev, B.B. Adsorption of proteins on gold nanoparticles: One or more layers? *Colloids Surf. B Biointerfaces* **2019**, *173*, 557–563. [[CrossRef](#)] [[PubMed](#)]
16. Sotnikov, D.V.; Byzova, N.A.; Zherdev, A.V.; Dzantiev, B.B. Retention of Activity by Antibodies Immobilized on Gold Nanoparticles of Different Sizes: Fluorometric Method of Determination and Comparative Evaluation. *Nanomaterials* **2021**, *11*, 3117. [[CrossRef](#)] [[PubMed](#)]
17. Dileseigres, A.S.; Prado, Y.; Pluchery, O. How to Use Localized Surface Plasmon for Monitoring the Adsorption of Thiol Molecules on Gold Nanoparticles? *Nanomaterials* **2022**, *12*, 292. [[CrossRef](#)]
18. Pan, Y.; Liu, X.; Qian, L.; Cui, Y.; Zheng, X.; Kang, Y.; Fu, X.; Wang, S.; Wang, P.; Wang, D. A hand-held optoelectronic tongue for the identification of heavy-metal ions. *Sens. Actuators B Chem.* **2022**, *352*, 130971. [[CrossRef](#)]

19. Cai, J.; Wu, X.; Li, S.; Zheng, F. Synthesis of TiO₂@WO₃/Au Nanocomposite Hollow Spheres with Controllable Size and High Visible-Light-Driven Photocatalytic Activity. *ACS Sustain. Chem. Eng.* **2016**, *4*, 1581–1590. [[CrossRef](#)]
20. Momeni, M.M.; Ghayeb, Y. Fabrication, characterization and photocatalytic properties of Au/TiO₂-WO₃ nanotubular composite synthesized by photo-assisted deposition and electrochemical anodizing methods. *J. Mol. Catal. A Chem.* **2016**, *417*, 107–115. [[CrossRef](#)]
21. Wang, X.; Pan, H.; Sun, M.; Zhang, Y. Au single atom-anchored WO₃/TiO₂ nanotubes for the photocatalytic degradation of volatile organic compounds. *J. Mater. Chem. A* **2021**, *10*, 6078–6085. [[CrossRef](#)]
22. Cao, Q.; Yuan, K.; Liu, Q.; Liang, C.; Wang, X.; Cheng, Y.F.; Li, Q.; Wang, M.; Che, R. Porous Au-Ag Alloy Particles Inlaid AgCl Membranes as Versatile Plasmonic Catalytic Interfaces with Simultaneous, in Situ SERS Monitoring. *ACS Appl. Mater. Interfaces* **2015**, *7*, 18491–18500. [[CrossRef](#)]
23. Cao, Q.; Liu, X.; Yuan, K.; Yu, J.; Liu, Q.; Delaunay, J.J.; Che, R. Gold nanoparticles decorated Ag(Cl,Br) micro-necklaces for efficient and stable SERS detection and visible-light photocatalytic degradation of Sudan I. *Appl. Catal. B Environ.* **2017**, *201*, 607–616. [[CrossRef](#)]
24. Cheng, Y.F.; Cao, Q.; Zhang, J.; Wu, T.; Che, R. Efficient photodegradation of dye pollutants using a novel plasmonic AgCl microrods array and photo-optimized surface-enhanced Raman scattering. *Appl. Catal. B Environ.* **2017**, *217*, 37–47. [[CrossRef](#)]
25. Zhou, L.; Zou, J.; Yu, M.; Lu, P.; Wei, J.; Qian, Y.; Wang, Y.; Yu, C. Green synthesis of hexagonal-shaped WO₃·0.33H₂O nanodiscs composed of nanosheets. *Cryst. Growth Des.* **2008**, *8*, 3993–3998. [[CrossRef](#)]
26. Shiraiishi, Y.; Hirakawa, H.; Togawa, Y.; Sugano, Y.; Ichikawa, S.; Hirai, T. Rutile crystallites isolated from degussa (Evonik) P25 TiO₂: Highly efficient photocatalyst for chemoselective hydrogenation of nitroaromatics. *ACS Catal.* **2013**, *3*, 2318–2326. [[CrossRef](#)]
27. Liu, X.; Zhang, J.; Yang, T.; Guo, X.; Wu, S.; Wang, S. Synthesis of Pt nanoparticles functionalized WO₃ nanorods and their gas sensing properties. *Sens. Actuators B Chem.* **2011**, *156*, 918–923. [[CrossRef](#)]
28. Theodorakopoulos, G.V.; Katsaros, F.K.; Papageorgiou, S.K.; Beazi-Katsioti, M.; Romanos, G.E. Engineering Commercial TiO₂ powder into Tailored Beads for Efficient Water Purification. *Materials* **2022**, *15*, 326. [[CrossRef](#)]
29. Scarpelli, F.; Mastropietro, T.F.; Poerio, T.; Godbert, N. Mesoporous TiO₂ Thin Films: State of the Art. In *Titanium Dioxide—Material for a Sustainable Environment*; Yang, D., Ed.; IntechOpen: Rijeka, Croatia, 2018.
30. Kong, Y.; Sun, H.; Fan, W.; Wang, L.; Zhao, H.; Zhao, X.; Yuan, S. Enhanced photoelectrochemical performance of tungsten oxide film by bifunctional Au nanoparticles. *RSC Adv.* **2017**, *7*, 15201–15210. [[CrossRef](#)]
31. Székely, I.; Kovács, G.; Baia, L.; Danciu, V.; Pap, Z. Synthesis of shape-tailored WO₃ micro-/nanocrystals and the photocatalytic activity of WO₃/TiO₂ composites. *Materials* **2016**, *9*, 258. [[CrossRef](#)] [[PubMed](#)]
32. Hatel, R.; Baitoul, M. Nanostructured tungsten trioxide (WO₃): Synthesis, structural and morphological investigations. *J. Phys. Conf. Ser.* **2019**, *1292*, 12014. [[CrossRef](#)]
33. Li, D.; Chen, S.; You, R.; Liu, Y.; Yang, M.; Cao, T.; Qian, K.; Zhang, Z.; Tian, J.; Huang, W. Titania-morphology-dependent dual-perimeter-sites catalysis by Au/TiO₂ catalysts in low-temperature CO oxidation. *J. Catal.* **2018**, *368*, 163–171. [[CrossRef](#)]
34. Chen, S.; Li, D.; Cao, T.; Huang, W. Size-Dependent Structures and Catalytic Performances of Au/TiO₂-{001} Catalysts for Propene Epoxidation. *J. Phys. Chem. C* **2020**, *124*, 15264–15274. [[CrossRef](#)]
35. Pang, Q.; Zhong, X.; Yan, W.; Ma, H.; Ren, H.; Song, L.; Lv, Z.; Li, L.; Chen, C.; Wang, H.; et al. Role of percentage of {001} crystal facets in TiO₂ supports toward the water-gas shift reaction over Au-TiO₂ catalysts. *Chem. Eng. J.* **2022**, *446*, 137010. [[CrossRef](#)]
36. Paradowska, E.; Arkusz, K.; Pijanowska, D.G. Comparison of Gold Nanoparticles Deposition Methods and Their Influence on Electrochemical and Adsorption Properties of Titanium Dioxide Nanotubes. *Materials* **2020**, *13*, 4269. [[CrossRef](#)] [[PubMed](#)]
37. Tada, K.; Maeda, Y.; Koga, H.; Okumura, M. TiO₂ Crystal Structure Dependence of Low-temperature CO Oxidation Catalyzed by Au/TiO₂. *Chem. Lett.* **2018**, *47*, 200–203. [[CrossRef](#)]
38. Tang, Y.; Chen, Y.; Liu, X.; Wang, C.; Zhao, Y.; Chen, R.; Shan, B. Facet-dependent activity of shape-controlled TiO₂ supported Au nanoparticles for the water-gas shift reaction. *Catal. Sci. Technol.* **2022**, *12*, 1530–1538. [[CrossRef](#)]
39. Yang, G.; Zhu, X.; Cheng, G.; Chen, R.; Xiong, J.; Li, W.; Wei, Y. Engineered tungsten oxide-based photocatalysts for CO₂ reduction: Categories and roles. *J. Mater. Chem. A* **2021**, *9*, 22781–22809. [[CrossRef](#)]
40. Pap, Z.; Tóth, Z.R.; Danciu, V.; Baia, L.; Kovács, G. Differently Shaped Au Nanoparticles: A Case Study on the Enhancement of the Photocatalytic Activity of Commercial TiO₂. *Materials* **2015**, *8*, 162–180. [[CrossRef](#)]
41. Martins, P.; Kappert, S.; Nga Le, H.; Sebastian, V.; Kühn, K.; Alves, M.; Pereira, L.; Cuniberti, G.; Melle-Franco, M.; Lanceros-Méndez, S. Enhanced Photocatalytic Activity of Au/TiO₂ Nanoparticles against Ciprofloxacin. *Catalysts* **2020**, *10*, 234. [[CrossRef](#)]
42. Chen, T.M.; Xu, G.Y.; Ren, H.; Zhang, H.; Tian, Z.Q.; Li, J.F. Synthesis of Au@TiO₂ core-shell nanoparticles with tunable structures for plasmon-enhanced photocatalysis. *Nanoscale Adv.* **2019**, *1*, 4522–4528. [[CrossRef](#)] [[PubMed](#)]
43. Yan, J.; Wu, G.; Guan, N.; Li, L.; Li, Z.; Cao, X. Understanding the effect of surface/bulk defects on the photocatalytic activity of TiO₂: Anatase versus rutile. *Phys. Chem. Chem. Phys.* **2013**, *15*, 10978–10988. [[CrossRef](#)]
44. Alotaibi, A.M.; Sathasivam, S.; Parkin, I.P. Aerosol assisted chemical vapour deposition of a ZrO₂-TiO₂ composite thin film with enhanced photocatalytic activity. *RSC Adv.* **2015**, *5*, 67944–67950. [[CrossRef](#)]
45. Anandan, S.; Wu, J.J. Ultrasound assisted synthesis of TiO₂-WO₃ heterostructures for the catalytic degradation of Tergitol (NP-9) in water. *Ultrason. Sonochem.* **2014**, *21*, 1284–1288. [[CrossRef](#)] [[PubMed](#)]

46. Baba, K.; Bulou, S.; Quesada-Gonzalez, M.; Bonot, S.; Collard, D.; Boscher, N.D.; Choquet, P. Significance of a Noble Metal Nanolayer on the UV and Visible Light Photocatalytic Activity of Anatase TiO₂ Thin Films Grown from a Scalable PECVD/PVD Approach. *ACS Appl. Mater. Interfaces* **2017**, *9*, 41200–41209. [[CrossRef](#)]
47. Green, S.V.; Kuzmin, A.; Purans, J.; Granqvist, C.G.; Niklasson, G.A. Structure and composition of sputter-deposited nickel-tungsten oxide films. *Thin Solid Film.* **2011**, *519*, 2062–2066. [[CrossRef](#)]
48. Cui, Y.; Pan, L.; Chen, Y.; Afzal, N.; Ullah, S.; Liu, D.; Wang, L.; Zhang, X.; Zou, J.J. Defected ZnWO₄-decorated WO₃ nanorod arrays for efficient photoelectrochemical water splitting. *RSC Adv.* **2019**, *9*, 5492–5500. [[CrossRef](#)]
49. Mohan, V.V.; Anjana, P.M.; Rakhi, R.B. A study on the effect of phase conversion of tungsten nanostructures on their electrochemical energy storage performance. *Mater. Adv.* **2022**, *3*, 5900–5910. [[CrossRef](#)]
50. Zeng, N.; Wang, Y.C.; Neilson, J.; Fairclough, S.M.; Zou, Y.; Thomas, A.G.; Cernik, R.J.; Haigh, S.J.; Lewis, D.J. Rapid and Low-Temperature Molecular Precursor Approach toward Ternary Layered Metal Chalcogenides and Oxides: Mo_{1-x}W_xS₂ and Mo_{1-x}W_xO₃ Alloys (0 ≤ x ≤ 1). *Chem. Mater.* **2020**, *32*, 7895–7907. [[CrossRef](#)] [[PubMed](#)]
51. Leghari, S.A.K.; Sajjad, S.; Chen, F.; Zhang, J. WO₃/TiO₂ composite with morphology change via hydrothermal template-free route as an efficient visible light photocatalyst. *Chem. Eng. J.* **2011**, *166*, 906–915. [[CrossRef](#)]
52. Stefanov, P.; Shipochka, M.; Stefchev, P.; Raicheva, Z.; Lazarova, V.; Spassov, L. XPS characterization of TiO₂ layers deposited on quartz plates. *J. Phys. Conf. Ser.* **2008**, *100*, 012039. [[CrossRef](#)]
53. Jaleh, B.; Etivand, E.S.; Mohazzab, B.F.; Nasrollahzadeh, M.; Varma, R.S. Improving wettability: Deposition of TiO₂ nanoparticles on the O₂ plasma activated polypropylene membrane. *Int. J. Mol. Sci.* **2019**, *20*, 3309. [[CrossRef](#)]
54. Zhao, B.; Zhang, X.; Mao, J.; Wang, Y.; Zhang, G.; Zhang, Z.C.; Guo, X. Crystal-Plane-Dependent Guaiacol Hydrodeoxygenation Performance of Au on Anatase TiO₂. *Catalysts* **2023**, *13*, 699. [[CrossRef](#)]
55. Leung, D.Y.C.; Fu, X.; Ye, D.; Huang, H. Effect of oxygen mobility in the lattice of Au/TiO₂ on formaldehyde oxidation. *Kinet. Catal.* **2012**, *53*, 239–246. [[CrossRef](#)]
56. Székely, I.; Baia, M.; Magyari, K.; Boga, B.; Pap, Z. The effect of the pH adjustment upon the WO₃-WO₃·0.33H₂O-TiO₂ ternary composite systems' photocatalytic activity. *Appl. Surf. Sci.* **2019**, *490*, 469–480. [[CrossRef](#)]
57. Kedves, E.-Z.; Székely, I.; Baia, L.; Baia, M.; Csavdári, A.; Pap, Z. The Comparison of the Photocatalytic Performance Shown by TiO₂ and TiO₂/WO₃ Composites—A Parametric and Kinetic Study. *J. Nanosci. Nanotechnol.* **2018**, *19*, 356–365. [[CrossRef](#)] [[PubMed](#)]
58. Székely, I.; Kedves, E.-Z.; Pap, Z.; Baia, M. Synthesis Design of Electronegativity Dependent WO₃ and WO₃·0.33H₂O Materials for a Better Understanding of TiO₂/WO₃ Composites' Photocatalytic Activity. *Catalysts* **2021**, *11*, 779. [[CrossRef](#)]
59. Boga, B.; Székely, I.; Focșan, M.; Baia, M.; Szabó, T.; Nagy, L.; Pap, Z. Sensor surface via inspiration from Nature: The specific case of electron trapping in TiO₂/WO₃(·0.33H₂O) and reaction center/WO₃(·0.33H₂O) systems. *Appl. Surf. Sci.* **2022**, *572*, 151139. [[CrossRef](#)]
60. Tóth, Z.R.; Debreczeni, D.; Gyulavári, T.; Székely, I.; Todea, M.; Kovács, G.; Focșan, M.; Magyari, K.; Baia, L.; Pap, Z.; et al. Rapid Synthesis Method of Ag₃PO₄ as Reusable Photocatalytically Active Semiconductor. *Nanomaterials* **2023**, *13*, 89. [[CrossRef](#)] [[PubMed](#)]
61. Bakar, S.K.; Niazi, S. Stability of aspirin in different media. *J. Pharm. Sci.* **1983**, *72*, 1024–1026. [[CrossRef](#)]
62. Skibinski, R.; Komsta, L. The stability and degradation kinetics of acetylsalicylic acid in different organic solutions revisited—An UHPLC-ESI-QTOF spectrometry study. *Curr. Issues Pharm. Med. Sci.* **2016**, *29*, 39–41. [[CrossRef](#)]
63. Boga, B.; Székely, I.; Pap, Z.; Baia, L.; Baia, M. Detailed Spectroscopic and Structural Analysis of TiO₂/WO₃ Composite Semiconductors. *J. Spectrosc.* **2018**, *2018*, 6260458. [[CrossRef](#)]
64. Chen, Z.; Fu, M.L.; Huang, X.D.; Yuan, B.; Yang, J.C.E. Magnetic infrared responsive photocatalyst: Fabrication, characterization, and photocatalytic performance of β-NaYF₄:Yb³⁺,Tm³⁺/TiO₂/Fe₃O₄@SiO₂ composite. *Res. Chem. Intermed.* **2018**, *44*, 6369–6385. [[CrossRef](#)]
65. Luna-Flores, A.; Sosa-Sánchez, J.L.; Morales-Sánchez, M.A.; Agustín-Serrano, R.; Luna-López, J.A. An easy-made, economical and efficient carbon-doped amorphous TiO₂ photocatalyst obtained by microwave assisted synthesis for the degradation of Rhodamine B. *Materials* **2017**, *10*, 1447. [[CrossRef](#)]
66. Movlaee, K.; Periasamy, P.; Krishnakumar, T.; Ganjali, M.R.; Leonardi, S.G.; Neri, G.; Chavali, M.; Siril, P.F.; Devarajan, V.P. Microwave-assisted synthesis and characterization of WO_x nanostructures for gas sensor application. *J. Alloys Compd.* **2018**, *762*, 745–753. [[CrossRef](#)]
67. Choy, J.H.; Kim, Y.I.; Yoon, J.B.; Choy, S.H. Temperature-dependent structural evolution and electrochromic properties of peroxopolytungstic acid. *J. Mater. Chem.* **2001**, *11*, 1506–1513. [[CrossRef](#)]
68. Yuksel, R.; Durucan, C.; Unalan, H.E. Ternary nanocomposite SWNT/WO₃/PANI thin film electrodes for supercapacitors. *J. Alloys Compd.* **2016**, *658*, 183–189. [[CrossRef](#)]
69. Kalaiarasi, S.; Jose, M. Streptomycin loaded TiO₂ nanoparticles: Preparation, characterization and antibacterial applications. *J. Nanostructure Chem.* **2017**, *7*, 47–53. [[CrossRef](#)]
70. Maulidiyah; Wibowo, D.; Hikmawati; Salamba, R.; Nurdin, M. Preparation and characterization of activated carbon from coconut shell-doped TiO₂ in water medium. *Orient. J. Chem.* **2015**, *31*, 2337–2342. [[CrossRef](#)]

71. Kedves, E.-Z.; Fodor, C.; Fazekas, Á.; Székely, I.; Szamosvölgyi, Á.; Sápi, A.; Kónya, Z.; Cristian Pop, L.; Baia, L.; Pap, Z. α -MoO₃ with inhibitive properties in Fenton reactions and insights on its general impact on OH radical based advanced oxidation processes. *Appl. Surf. Sci.* **2023**, *624*, 156914. [[CrossRef](#)]
72. Kedves, E.-Z.; Bárdos, E.; Ravasz, A.; Tóth, Z.-R.; Mihálydeákpál, S.; Kovács, Z.; Pap, Z.; Baia, L. Photoinhibitive Properties of α -MoO₃ on Its Composites with TiO₂, ZnO, BiOI, AgBr, and Cu₂O. *Materials* **2023**, *16*, 3621. [[CrossRef](#)] [[PubMed](#)]
73. Fateixa, S.; Nogueira, H.I.S.; Trindade, T. Surface-Enhanced Raman Scattering Spectral Imaging for the Attomolar Range Detection of Crystal Violet in Contaminated Water. *ACS Omega* **2018**, *3*, 4331–4341. [[CrossRef](#)]
74. Wu, J.; Yang, X.; Fang, J. Convective combined interfacial assembly of surfactantless ordered Au nanoparticles and SERS performance. *J. Nanoparticle Res.* **2019**, *21*, 78. [[CrossRef](#)]
75. Cañamares, M.V.; Chenal, C.; Birke, R.L.; Lombardi, J.R. DFT, SERS, and single-molecule SERS of crystal violet. *J. Phys. Chem. C* **2008**, *112*, 20295–20300. [[CrossRef](#)]
76. Wang, J.; Gao, X.; Sun, H.; Su, B.; Gao, C. Monodispersed graphene quantum dots encapsulated Ag nanoparticles for surface-enhanced Raman scattering. *Mater. Lett.* **2016**, *162*, 142–145. [[CrossRef](#)]
77. Lin, S.C.; Zhang, X.; Zhao, W.C.; Chen, Z.Y.; Du, P.; Zhao, Y.M.; Wu, Z.L.; Xu, H.J. Quantitative and sensitive detection of prohibited fish drugs by surface-enhanced Raman scattering. *Chin. Phys. B* **2018**, *27*, 028707. [[CrossRef](#)]
78. Morovvati, B.; Malekfar, R. Surface Enhanced Raman Scattering of Crystal Violet with Low Concentrations Using Self-Assembled Silver and Gold-Silver Core-Shell Nanoparticles. *Int. J. Opt. Photonics* **2019**, *13*, 89–96. [[CrossRef](#)]
79. Škrabić, M.; Kosović, M.; Gotić, M.; Mikac, L.; Ivanda, M.; Gamulin, O. Near-infrared surface-enhanced raman scattering on silver-coated porous silicon photonic crystals. *Nanomaterials* **2019**, *9*, 421. [[CrossRef](#)]
80. Ma, H.; Xu, L.; Tian, Y.; Jiao, A.; Zhang, M.; Li, S.; Chen, M. Design of a thermally stable and highly active SERS optical sensor for the ultrasensitive detection of dye molecules at high-temperature. *Opt. Mater. Express* **2021**, *11*, 2001. [[CrossRef](#)]
81. Smitha, S.L.; Gopchandran, K.G.; Smijesh, N.; Philip, R. Size-dependent optical properties of Au nanorods. *Prog. Nat. Sci. Mater. Int.* **2013**, *23*, 36–43. [[CrossRef](#)]
82. Camerlingo, C.; Portaccio, M.; d’Apuzzo, F.; Nucci, L.; Perillo, L.; Lepore, M. μ -FTIR, μ -Raman, and SERS Analysis of Amide I Spectral Region in Oral Biofluid Samples during Orthodontic Treatment. *Sensors* **2022**, *22*, 7874. [[CrossRef](#)] [[PubMed](#)]
83. Xue, L.; Yan, B.; Li, Y.; Tan, Y.; Luo, X.; Wang, M. Surface-enhanced raman spectroscopy of blood serum based on gold nanoparticles for tumor stages detection and histologic grades classification of oral squamous cell carcinoma. *Int. J. Nanomed.* **2018**, *13*, 4977–4986. [[CrossRef](#)] [[PubMed](#)]
84. Indrasekara, A.S.D.S.; Thomas, R.; Fabris, L. Plasmonic properties of regiospecific core-satellite assemblies of gold nanostars and nanospheres. *Phys. Chem. Chem. Phys.* **2014**, *17*, 21133–21142. [[CrossRef](#)] [[PubMed](#)]
85. Pattabiraman, V.R.; Bode, J.W. Rethinking amide bond synthesis. *Nature* **2011**, *480*, 471–479. [[CrossRef](#)] [[PubMed](#)]
86. Alfano, A.I.; Lange, H.; Brindisi, M. Amide Bonds Meet Flow Chemistry: A Journey into Methodologies and Sustainable Evolution. *ChemSusChem* **2022**, *15*, e202102708. [[CrossRef](#)] [[PubMed](#)]
87. Darienzo, R.E.; Chen, O.; Sullivan, M.; Mironava, T.; Tannenbaum, R. Au nanoparticles for SERS: Temperature-controlled nanoparticle morphologies and their Raman enhancing properties. *Mater. Chem. Phys.* **2020**, *240*, 122143. [[CrossRef](#)]
88. Nikoobakht, B.; Burda, C.; Braun, M.; Hun, M.; El-Sayed, M.A. The Quenching of CdSe Quantum Dots Photoluminescence by Gold Nanoparticles in Solution. *Photochem. Photobiol.* **2002**, *75*, 591. [[CrossRef](#)] [[PubMed](#)]
89. Vilela, D.; Cristina González, M.; Escarpa, A. Gold-nanosphere formation using food sample endogenous polyphenols for in-vitro assessment of antioxidant capacity. *Anal. Bioanal. Chem.* **2012**, *404*, 341–349. [[CrossRef](#)] [[PubMed](#)]
90. Kang, M.; Liang, J.; Wang, F.; Chen, X.; Lu, Y.; Zhang, J. Structural design of hexagonal/monoclinic WO₃ phase junction for photocatalytic degradation. *Mater. Res. Bull.* **2020**, *121*, 110614. [[CrossRef](#)]
91. Jaiswal, M.K.; Choudhury, B. Hydrated Orthorhombic/Hexagonal Mixed-Phase WO₃ Core-Shell Nanoribbons for Hole-Mediated Photocatalysis. *ACS Appl. Nano Mater.* **2022**, *5*, 3599–3610. [[CrossRef](#)]
92. Lin, R.; Wan, J.; Xiong, Y.; Wu, K.; Cheong, W.; Zhou, G.; Wang, D.; Peng, Q.; Chen, C.; Li, Y. Quantitative Study of Charge Carrier Dynamics in Well-Defined WO₃ Nanowires and Nanosheets: Insight into the Crystal Facet Effect in Photocatalysis. *J. Am. Chem. Soc.* **2018**, *140*, 9078–9082. [[CrossRef](#)] [[PubMed](#)]
93. Enesca, A.; Isac, L. The influence of light irradiation on the photocatalytic degradation of organic pollutants. *Materials* **2020**, *13*, 2494. [[CrossRef](#)] [[PubMed](#)]

Disclaimer/Publisher’s Note: The statements, opinions and data contained in all publications are solely those of the individual author(s) and contributor(s) and not of MDPI and/or the editor(s). MDPI and/or the editor(s) disclaim responsibility for any injury to people or property resulting from any ideas, methods, instructions or products referred to in the content.